ALMA observations of the Extended Green Object G19.01–0.03: I. A Keplerian disc in a massive protostellar system

G. M. Williams,[1,2]★ C. J. Cyganowski,[3] C. L. Brogan,[4] T. R. Hunter,[4] J. D. Ilee,[2] P. Nazari,[5] J. M. D. Kruijssen,[6] R. J. Smith[7] and I. A. Bonnell[3]

[1]*Centre for Astrophysics Research, Department of Physics, Astronomy and Mathematics, University of Hertfordshire, College Lane, Hatfield, AL10 9AB, UK*
[2]*School of Physics & Astronomy, The University of Leeds, Leeds, LS2 9JT, UK*
[3]*Scottish Universities Physics Alliance (SUPA), School of Physics and Astronomy, University of St Andrews, North Haugh, St Andrews, KY16 9SS, UK*
[4]*National Radio Astronomy Observatory (NRAO), 520 Edgemont Rd, Charlottesville, VA 22903, USA*
[5]*Leiden Observatory, Leiden University, PO Box 9513, 2300 RA Leiden, NL*
[6]*Astronomisches Rechen-Institut, Zentrum für Astronomie der Universität Heidelberg, Mönchhofstraße 12-14, 69120 Heidelberg, DE*
[7]*Jodrell Bank Centre for Astrophysics, Department of Physics and Astronomy, University of Manchester, Oxford Road, Manchester, M13 9PL, UK*

arXiv:2110.06262v1 [astro-ph.GA] 12 Oct 2021

Accepted XXX. Received YYY; in original form ZZZ

ABSTRACT

Using the Atacama Large Millimetre/submillimeter Array (ALMA) and the Karl G. Jansky Very Large Array (VLA), we observed the Extended Green Object (EGO) G19.01–0.03 with sub-arcsecond resolution from 1.05 mm to 5.01 cm wavelengths. Our ∼ 0.4″ ∼ 1600 AU angular resolution ALMA observations reveal a velocity gradient across the millimetre core MM1, oriented perpendicular to the previously known bipolar molecular outflow, that is consistently traced by 20 lines of 8 molecular species with a range of excitation temperatures, including complex organic molecules (COMs). Kinematic modelling shows the data are well described by models that include a disc in Keplerian rotation and infall, with an enclosed mass of 40 – 70 $M_\odot$ (within a 2000 AU outer radius) for a disc inclination angle of $i = 40°$, of which 5.4 – 7.2 $M_\odot$ is attributed to the disc. Our new VLA observations show that the 6.7 GHz Class II methanol masers associated with MM1 form a partial ellipse, consistent with an inclined ring, with a velocity gradient consistent with that of the thermal gas. The disc-to-star mass ratio suggests the disc is likely to be unstable and may be fragmenting into as-yet-undetected low mass stellar companions. Modelling the centimetre–millimetre spectral energy distribution of MM1 shows the ALMA 1.05 mm continuum emission is dominated by dust, whilst a free-free component, interpreted as a hypercompact HII region, is required to explain the VLA ∼5 cm emission. The high enclosed mass derived for a source with a moderate bolometric luminosity (∼10^4 $L_\odot$) suggests that the MM1 disc may feed an unresolved high-mass binary system.

Key words: stars: individual: G19.01–0.03 – stars: formation – stars: massive – stars: protostars – masers – techniques: interferometric

1 INTRODUCTION

Both theory and observations suggest that in the low- to intermediate-mass regime ($M_* < 8\,M_\odot$), protostars accrete material through rotationally supported circumstellar accretion discs and shed excess angular momentum through bipolar outflows (e.g. Zinnecker & Yorke 2007). In the high-mass regime ($M_* > 8\,M_\odot$), scaling up this process creates an effective pathway for overcoming the hindering effects of high radiation pressure and stellar winds to enable the growth of massive young stellar objects (MYSOs; e.g. Krumholz et al. 2009; Kuiper et al. 2011; Klassen et al. 2016; Rosen et al. 2016, 2019; Meyer et al. 2018; Kuiper & Hosokawa 2018; Mignon-Risse et al. 2021). MYSOs are indeed commonly observed with active outflows (e.g. Beuther et al. 2002), however observations of the accompanying circumstellar discs are comparatively lacking. This may be partly attributed to regions of high-mass star formation being several kpc distant and more clustered than their lower mass counterparts. Moreover, the short pre-main sequence lifetimes of high-mass stars (< 1 Myr, e.g. Mottram et al. 2011) mean they remain embedded within regions of high extinction in their natal molecular clouds for the duration of their formation (e.g. Kruijssen et al. 2019; Chevance et al. 2020; Kim et al. 2020). High angular resolution studies at (sub)millimetre wavelengths now have the ability to resolve and disentangle thermal emission in these distant, clustered and embedded environments. Most disc candidates around high-mass protostars have been observed towards proto-B stars (e.g. Cesaroni et al. 2007; Sánchez-Monge et al. 2013; Cesaroni et al. 2014; Beltrán et al. 2014; Beltrán & de Wit 2016; Girart et al. 2017; Añez-López et al. 2020; Jiménez-Serra et al. 2020), with relatively few candidate discs observed towards proto-O stars, e.g. AFGL 2591 VLA 3 (Jiménez-Serra et al. 2012), NGC 6334 I(N) (Hunter et al. 2014), IRAS 16547-4247 (Zapata et al. 2015, 2019), AFGL 4176 (Johnston et al. 2015, 2020), AFGL 2136 (Maud et al. 2018, 2019), G11.92–0.61 MM1 (Ilee et al. 2016, 2018), G023.01–0.41 (Sanna et al. 2019), G345.50+0.35 M, G345.50+0.35

★ E-mail: G.M.Williams@leeds.ac.uk

© 2021 The Authors

S and G29.96–0.02 (Cesaroni et al. 2017), with central protostellar masses ~10–45 $M_\odot$ and luminosities of $(0.1 - 5.8) \times 10^5$ $L_\odot$.

In the search for circumstellar discs around high-mass protostars, Extended Green Objects (EGOs; Cyganowski et al. 2008, 2009) may represent excellent candidate hosts. EGOs are characterised by extended 4.5μm emission in *Spitzer* GLIMPSE images (Benjamin et al. 2003; Churchwell et al. 2009) that is thought to trace shocked gas in molecular outflows. EGOs are also strongly associated both with radiatively-pumped 6.7 GHz Class II CH_3OH masers, which are known to exclusively trace high-mass star formation (e.g. Cragg et al. 2005; Billington et al. 2019; Jones et al. 2020), and with collisionally-pumped 44 and 25 GHz Class I CH_3OH masers (e.g. Cyganowski et al. 2008, 2009; Towner et al. 2017). On the whole, EGOs can be inferred to contain one (or more) MYSOs that have active outflows and hence exist in a stage of ongoing accretion.

In this series of papers, we present Atacama Large Millimetre/submillimetre Array (ALMA) Cycle 2 observations of the EGO G19.01–0.03 (hereafter G19.01) in Band 7 at 1.05 mm with ~ 0.″4 resolution, the highest resolution observations of this source presented to date. Figure 1 presents an overview of previous (sub)millimetre observations of G19.01. The millimetre core MM1 appeared as a single millimetre continuum source in 1.3 mm Submillimeter Array (SMA) and 3.4 mm Combined Array for Research in Millimeter-wave Astronomy (CARMA) observations (angular resolution 2.″3 and 5.″4 respectively; Cyganowski et al. 2011a). The 1.3 mm and 3.4 mm continuum peaks are coincident with each other, and with 6.7 GHz Class II CH_3OH maser emission (Cyganowski et al. 2009, 2011a). Larger scale emission from the surrounding clump is detected in both 870 μm ATLASGAL (Schuller et al. 2009, see Figure 1) and 1.1 mm Bolocam Galactic Plane Survey (BGPS; Rosolowsky et al. 2010) observations. From the 1.3 mm SMA continuum emission, Cyganowski et al. (2011a) calculated a gas mass of 12 – 16 $M_\odot$ for MM1 for $T_{\rm dust}$ = 130 – 100 K (based on CH_3CN(J=12–11) fitting). A remarkably collimated, high velocity bipolar outflow is observed emanating from MM1 in ^{12}CO(2–1) with the SMA (see Figure 1) and is also detected in HCO^+(1–0) and SiO(2–1) emission with CARMA. The lobes of this outflow are also traced by 44 GHz Class I CH_3OH masers (Figure 1; Cyganowski et al. 2009, 2011a). At the sensitivity level of the SMA and CARMA, MM1 appeared to be lacking in chemical richness. Complex organic molecules (COMs), defined as carbon-bearing molecules with six or more atoms, are recognised as tracers of high-mass star formation and of hot core MYSOs (e.g. Herbst & van Dishoeck 2009). In the SMA and CARMA observations, only two COMs were detected towards MM1: CH_3OH and CH_3CN (Cyganowski et al. 2011a). No 3.6 cm or 1.3 cm continuum emission was detected towards MM1 in deep, arcsecond-resolution VLA observations (4σ limits 0.12 and 1.04 mJy beam^{-1}, respectively), implying a low ionising luminosity ($N_{\rm Lyc} < 2.0 \times 10^{45}$ s^{-1}) or very small (diameter <80 AU) H II region (Cyganowski et al. 2011b). The bolometric luminosity of MM1, estimated by fitting the mid-infrared (MIR) to millimetre spectral energy distribution (SED), is moderate, ~ 10^4 $L_\odot$ (Cyganowski et al. 2011a, see also Cyganowski et al. 2011b). In all, these signatures indicate that MM1 is a young millimetre source at an early stage of evolution that is undergoing active accretion, with the highly collimated outflow suggesting that MM1 is an excellent target in the search for discs around MYSOs.

In this paper (Paper I), we present an analysis of the kinematics and the centimetre-millimetre wavelength SED of G19.01–0.03 MM1. In Section 2 we describe the observations and in Section 3 we present the results for the continuum and the molecular line kinematics. Section 4 presents our kinematic and SED modelling and discusses the implications of our results for the stability of the MM1 disc and the nature of the central source(s). Section 5 summarises our main conclusions. Throughout, we adopt a near kinematic distance of 4.0 ± 0.3 kpc, estimated from the NH_3 LSRK velocity from Cyganowski et al. (2013) and the Galactic rotation curve parameters from Reid et al. (2014).

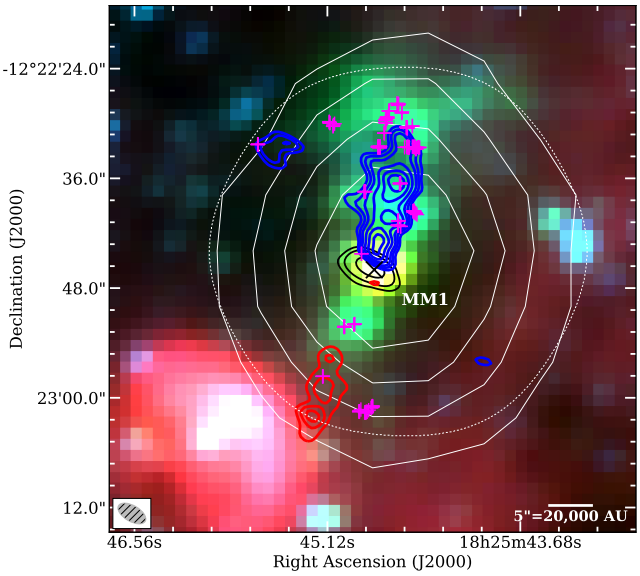


Figure 1. *Spitzer* GLIMPSE three-colour image (RGB: 8.0, 4.5, 3.6μm), overlaid with contours of SMA 1.3 mm continuum (black: [5, 10, 30]×σ, where 1σ = 3.5 mJy beam^{-1}) and high-velocity blue- and redshifted ^{12}CO(2 – 1) emission (blue: 7.2, 9.6, 12.0, 15.6, 19.2, 22.8 Jy beam^{-1} km s^{-1}; red: 4.8, 7.2, 9.6 Jy beam^{-1} km s^{-1}) from Cyganowski et al. (2011a). Positions of 44 GHz Class I CH_3OH masers from Cyganowski et al. (2009) are marked by magenta +, and their intensity-weighted 6.7 GHz Class II CH_3OH maser position is marked with a black ×. Contours of the ATLASGAL 870μm emission (resolution 18″; Schuller et al. 2009) (solid white: [12, 16, 20, 24]×σ, where 1σ = 0.08 Jy beam^{-1}) and the 30 per cent response level of the ALMA mosaic (dotted white) are also overlaid. The SMA beam is shown at bottom left.

2 OBSERVATIONS

2.1 Atacama Large Millimetre/submillimetre Array (ALMA)

Our ALMA Cycle 2 observations (PI: C. Cyganowski; 2013.1.00812.S) mapped G19.01–0.03 at 1.05 mm with a 7–pointing mosaic. The ALMA mosaic is ~40″ wide (to the 30 per cent response level), equivalent to ~0.78 pc at a distance of 4 kpc. The coverage of the ALMA mosaic is shown in Figure 1; observing parameters are given in Table 1.

The ALMA correlator configuration included seven spectral windows (spws): two broad spws with relatively coarse spectral resolution (Table 1), centred at ~278.2 GHz and ~292.0 GHz, and five narrow spws targeting specific spectral lines. Four of the narrow spws have bandwidths of 117.2 MHz (~121 km s^{-1}) and were tuned to cover H_2CO $4_{0,4} - 3_{0,3}$ at 290.62341 GHz, DCN (4–3) at 289.64492 GHz, $C^{33}S$ (6–5) at 291.48593 GHz and ^{34}SO 6_7–5_6 at 290.56224 GHz; the remaining narrow spw has a bandwidth of 468.8 MHz (~503 km s^{-1}) and was tuned to cover N_2H^+(3–2) at

Table 1. Observing parameters of the new data used.

Parameter	ALMA 1.05 mm	VLA 1.21 cm	VLA 5.01 cm
Observing date	14 May 2015	11-12 Nov 2013	3 Feb 2014
On-source integration time	44 min	139 min	47 min
Number of antennas	37	25	27
Antenna configuration	C43-3/(4)	B	BnA
Phase Centre (J2000):			
R.A. ($^{\rm h\,m\,s}$)	18:25:44.61[a]	18:25:44.80	18:25:44.80
Dec. ($^\circ\ '\ ''$)	-12:22:44.00[a]	-12:22:46.00	-12:22:46.00
Projected baseline lengths	20–533 m	0.14–9.98 km	0.26–16.54 km
	19–508 $k\lambda$	12–825 $k\lambda$	5–330 $k\lambda$
Mean frequency[b]	285.12 GHz	24.81 GHz	5.99 GHz
Mean wavelength[b]	1.05 mm	1.21 cm	5.01 cm
Primary beam FWHP[c]	n/a (mosaic)	1.8′	7.5′
Synthesised beam[b]	0.″52 × 0.″35	0.″33 × 0.″22	0.″91 × 0.″49
Beam position angle[b,d]	88.4°	0.5°	73.4°
Maximum Recoverable Scale[e]	4.″2	4.″5	13.″0
Bandwidth[f]	2 × 1.875 GHz	16 × 0.128 GHz	16 × 0.128 GHz
Channel spacing[f]	0.977 MHz	1.000 MHz	1.000 MHz
Spectral line RMS noise[f,g]:	3.0 mJy beam^{-1}	n/a	n/a
Continuum RMS noise[h]	0.25 mJy beam^{-1}	6.0 μJy beam^{-1}	5.0 μJy beam^{-1}
Gain calibrator	J1733–1304	J1832–1035	J1832–1035
Bandpass calibrator	J1733–1304	J1924–2914	J1924–2914
Flux calibrator	Titan[i]	J1331+3030	J1331+3030

[a] For the central pointing of the mosaic.
[b] For the continuum image.
[c] At the mean frequency.
[d] Measured East of North i.e. positive in the anti-clockwise direction.
[e] Calculated from the fifth percentile shortest baseline (as stated in the ALMA Technical Handbook) and mean frequency, using `au.estimateMRS` from the analysisUtils Python package.
[f] For the two wide spectral windows (ALMA) and continuum spectral windows (VLA); see §2.1 and §2.2 for details of narrow spectral windows targeting specific spectral lines. For the ALMA wideband spws, the Hanning-smoothed spectral resolution is 1.156× the channel spacing due to online channel averaging in the ALMA correlator.
[g] Median value for emission-free channels, imaged with the native channel spacing, for lines presented in this paper. The rms noise is up to ∼1.5× higher in channels with complex emission.
[h] Estimated from emission-free regions within the 30% response level of the ALMA mosaic.
[i] Using Butler-JPL-Horizons 2012 models.

279.51176 GHz. For all 5 narrow spws, the (Hanning-smoothed) spectral resolution is 0.244 MHz.

The data were calibrated using the CASA 4.2.2 version of the ALMA calibration pipeline. Following application of the calibration, the science target fields were split off, and a pseudo-continuum data set constructed from line-free channels. In our ALMA data, G19.01−0.03 MM1 exhibits a line-rich hot core spectrum (§3.2); following the approach of Brogan et al. (2016); Cyganowski et al. (2017), we selected line-free channels using dirty line+continuum cubes. As in the Cyganowski et al. (2017) observations with the same tuning, identifying line-free channels in the narrow $C^{33}S$ spectral window (spw 3) was problematic due to wide lines and possible absorption features, and we excluded this spw from our aggregate continuum data set. The total bandwidth used for our final continuum image is ∼1.6 GHz.

The continuum data were iteratively self-calibrated and the solutions were applied to the line data. The final continuum image was made using multi-frequency synthesis and Briggs weighting with a robust parameter $R = 0$, yielding a synthesised beamsize of 0.″52×0.″35, equivalent to 2080×1400 AU at 4 kpc. In this paper, we primarily present line data from the two broad spws, as these account for the vast majority of the lines suitable for kinematic analysis (§3.2). Line image cubes were made with $R = 0.5$, and their synthesised beamsizes vary slightly as a function of frequency. For example, the synthesised beamsize is 0.″58 × 0.″41 (P.A.= 82.5°) for g-CH_3CH_2OH $16_{6,10}$–$15_{6,9}$ (v_t=0-0) at $\nu_{\rm rest}$ =277.41431 GHz, and 0.″55 × 0.″40 (P.A.= 82.5°) for CH_3OH (v_t=0) $6_{1,5}$–$5_{1,4}$ at $\nu_{\rm rest}$ =292.67291 GHz. Additional details are given in Table 1 for lines in the broad spws. One line that is suitable for kinematic analysis is serendipitously detected in a narrow spw (that targeting N_2H^+): CH_3OH (v_t=0) $11_{2,10}$–$10_{3,7}$ ($\nu_{\rm rest}$ =279.35189 GHz, E_u/k_B=190.9 K; Müller et al. 2001). This line was imaged with $R = 0.5$ and Δv = 0.25 km s^{-1}; the synthesised beamsize is 0.″57 × 0.″41 (P.A.= 83.0°) and the rms noise is ∼7.2 mJy beam^{-1}, measured in emission-free regions of channels with bright emission. All measurements were made from images corrected for the primary beam response.

2.2 Karl G. Jansky Very Large Array (VLA)

We observed G19.01–0.03 with the Karl G. Jansky Very Large Array (VLA) at 1.21 cm (K band) and 5.01 cm (C band), under project code 13B-359 (PI: T Hunter). In this paper, we consider only the continuum and 6.7 GHz CH_3OH maser data. Observational parameters and continuum image properties are given in Table 1. Both VLA datasets

were calibrated using the CASA 4.7.1 version of the VLA calibration pipeline and were Hanning smoothed.

The K band tuning included sixteen 0.128 GHz spectral windows for continuum, and narrower spectral windows targeting spectral lines including NH_3(J=K=1, 2, 3, 5, 6, 7). The NH_3(3,3) line exhibits maser behaviour in other EGOs (e.g. Brogan et al. 2011), and in our G19.01–0.03 data is strong enough to use for self-calibration. The NH_3(3,3) line was observed with an 8 MHz spectral window with 15.625 kHz channels. After continuum subtraction in the u, v-plane, we performed phase-only self-calibration using the channel with the strongest NH_3(3,3) emission, and applied the solutions to the continuum data (as well as to the line data, which are not considered further here). Channels in the continuum spws corresponding to the sky frequencies of targeted spectral lines were flagged prior to continuum imaging to remove line contamination. The 1.21 cm aggregate continuum was imaged using multi-frequency synthesis, two Taylor terms to account for the spectral index of the emission across the observed bandwidth and Briggs weighting with a robust parameter R = 0.5. The synthesised beamsize of 0.″33×0.″22 corresponds to 1320×880 AU at 4 kpc.

The C band tuning included sixteen 0.128 GHz spectral windows for continuum and one 2.0 MHz window with 3.906 kHz (~0.18 km s^{-1}) channels covering the 6.7 GHz Class II CH_3OH maser line. After continuum subtraction in the u, v-plane, the maser data were iteratively self-calibrated using the channel with the brightest maser emission; the solutions were also applied to the continuum data. The maser data were imaged with 0.3 km s^{-1} channels and Briggs weighting with a robust parameter R = 0. The resulting image cube has a synthesised beamsize of 0.″97 × 0.″38 (P.A. 76.3°) and a 1σ rms noise ranging from 1.85 mJy beam^{-1} in line-free channels to 5.35 mJy beam^{-1} in the channel with the strongest emission (see also §3.3). Channels in the continuum spws corresponding to the sky frequencies of emission lines expected in massive star forming regions (including the 6.7 GHz CH_3OH maser line) were flagged prior to continuum imaging to remove line contamination. The 5.01 cm aggregate continuum was imaged using multi-frequency synthesis, two Taylor terms to account for the spectral index of the emission across the observed bandwidth, and Briggs weighting with a robust parameter R = 0.5. An initial continuum image, made using all data, showed image artefacts from extended emission poorly sampled in our high-resolution data. To reduce these artefacts and improve our sensitivity to compact emission associated with G19.01–0.03, a u, v-range > 20$k\lambda$ was applied in making the final continuum image for which properties are quoted in Table 1. All measurements were made from images corrected for the primary beam response.

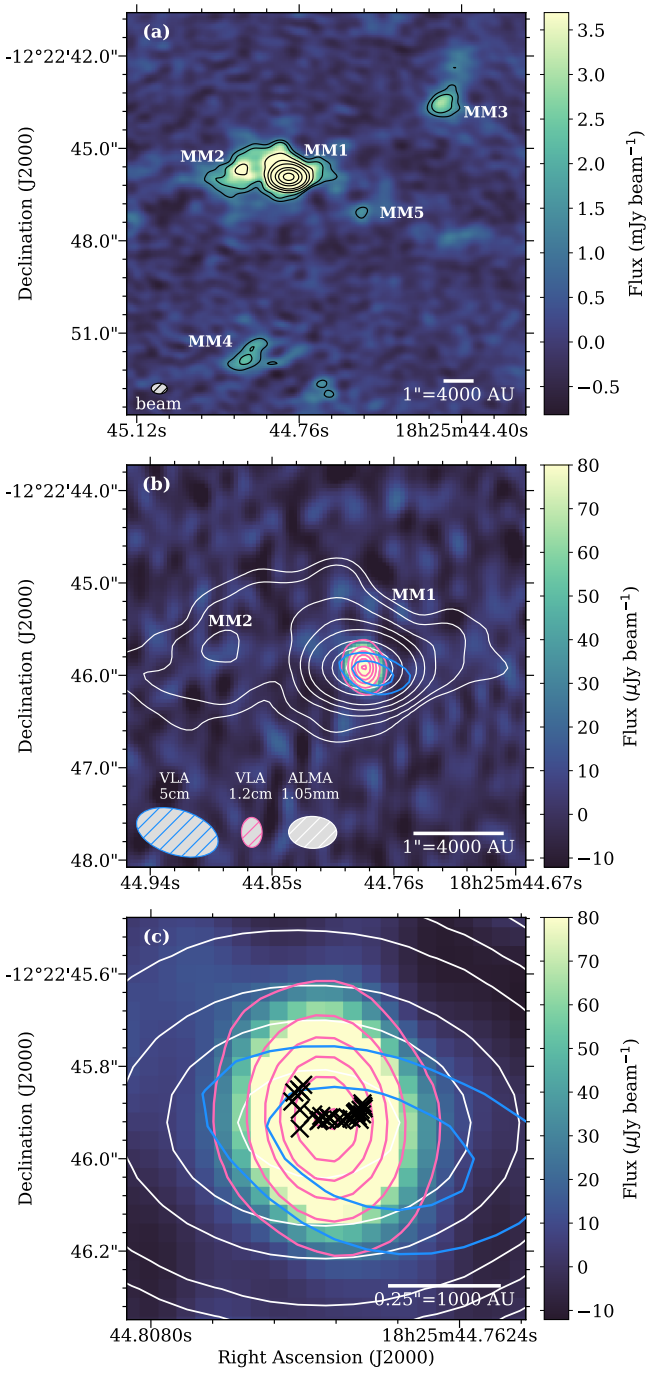


Figure 2. (a) ALMA 1.05 mm continuum image, corrected for the primary beam response, in linear colour scale. To emphasise the low-lying extended emission, the maximum colour scale is limited to 3.7 mJy beam^{-1}. The field of view shown is smaller than that of the mosaic, but includes all detected (≥5σ) emission. Black contours are plotted at 5, 8, 16, 32, 64, 200, 400 and 800σ, where σ = 0.25 mJy beam^{-1}. (b) Zoom view of the VLA 1.21 cm continuum emission (colour scale, and pink contours in 8σ steps from 4–44σ), overlaid with contours of the VLA 5.01 cm (blue: 4, 5σ) and ALMA 1.05 mm (white: 5, 8, 16, 32, 64, 200, 400, 800σ) continuum emission. The synthesised beams are plotted at lower left, and match the contour colours. MM3, MM4 and MM5 are outside the field of view shown. (c) Zoom view of (b), with new VLA 6.7 GHz Class II CH_3OH maser positions (Section 3.3) plotted as black ×.

3 RESULTS

3.1 Continuum emission

The ALMA 1.05 mm continuum image shows a strong continuum source at the known position of MM1, sitting within extended emission that is typically 100 times fainter in surface brightness than the MM1 peak (Figure 2a,b). Our deep ALMA continuum image also reveals a few new candidate neighbouring sources, with peak intensities at the level of a few mJy beam^{-1}. Whilst a single 2D Gaussian would reasonably reproduce the MYSO's bright compact emission, it could not account for the non-Gaussian low-lying extended emission. Dendrograms, in contrast, extract structures at regular isocontours of a map, and are typically used in the understanding of hierarchical structure (e.g. Goodman et al. 2009; Friesen et al.

Table 2. Observed continuum properties of MM1.

Tel. / λ	Mean freq. (GHz)	Source	J2000.0 Coordinates[a] α ($^{h\,m\,s}$)	δ ($^\circ\ '\ ''$)	Peak intensity[b] (mJy beam^{-1})	Integ. flux[b] (mJy)	Source size[c] Maj. × Min. [P.A.] ($''\times''[^\circ]$)	Source size (au)
ALMA 1.05 mm	285.115	MM1	18:25:44.782	-12:22:45.92	266.3	303.1	1.15 × 0.84 [78.7]	4600 × 3360
VLA 1.21 cm	24.806	CM1	18:25:44.7821	-12:22:45.913	0.271 ± 0.006	0.295 ± 0.011	< 0.13× < 0.03	< 520× < 120
VLA 5.01 cm	5.987	CM1	18:25:44.773	-12:22:46.00	0.029 ± 0.005	0.038 ± 0.011	0.4 × 0.32 [75]	1600 × 1280

[a] ALMA: peak position, VLA: centroid position from two-dimensional Gaussian fitting, see §3.1. The number of significant figures reflects a one pixel uncertainty (ALMA) or the statistical uncertainties from the Gaussian fitting (VLA).

[b] ALMA: evaluated within the intensity-weighted second moment size (not the total dendrogram structure). VLA: from two-dimensional Gaussian fits; statistical uncertainties are quoted.

[c] Major and minor axes sizes, deconvolved from the beam; position angle is measured East of North i.e. positive in the anti-clockwise direction. ALMA: sizes are calculated from the intensity-weighted second moment (HWHM, using ASTRODENDRO) converted to FWHM (and multiplied by $\sqrt{8\ln 2}$; shown in Figure 3). VLA: from two-dimensional Gaussian fitting. At 1.21 cm, CM1 is fit as a point source: the reported size is the upper limit from the CASA IMFIT task. At 5.01 cm, the fitted size is poorly constrained, with statistical uncertainties of 0.″4, 0.″09, and 23° for the major and minor axes and P.A., respectively.

2016; Kauffmann et al. 2017; Rigby et al. 2018; Williams et al. 2018; Watkins et al. 2019; Lu et al. 2020). We use the ASTRODENDRO Python package (Rosolowsky et al. 2008) to extract structures across the mosaic area, out to the 30 per cent response level (shown in Figure 1). The algorithm has three free parameters: the minimum isocontour value ($I_{\rm min}$), the minimum isocontour spacing that separates structures at different isocontours ($\Delta I_{\rm min}$), and the minimum size of a structure ($n_{\rm pix}$). We set these parameters to $I_{\rm min} = 5\sigma_{\rm rms} = 1.25$ mJy beam^{-1}, $\Delta I_{\rm min} = 1\sigma_{\rm rms} = 0.25$ mJy beam^{-1}, and $n_{\rm pix} = 25$ pixels $\approx n_{\rm pix,beam}/2$ (where $n_{\rm pix,beam}$ is the number of pixels in the ALMA synthesised beam) respectively. In effect, the wings of the emission profiles of extracted structures are clipped by the algorithm to $I_{\rm min}$ (see Rosolowsky et al. 2008). Whilst this does not have a significant impact on strong sources, it can lead to weak point sources being reported with sizes less than a beam. Setting the minimum source size to ~half a beam allows for the extraction of such weak sources despite this effect. The observed properties of MM1 obtained from the dendrogram analysis are listed in Table 2. Another four new millimetre sources are extracted in the field (named MM2...MM5, in order of decreasing peak intensity), possibly revealing the early stages of protocluster formation. The properties and nature of these sources will be discussed in Paper II (Williams et al. in prep.).

Our new 1.21 cm and 5.01 cm VLA images are presented in Figure 2b,c. As shown in Figure 2b, the centimetre emission associated with MM1 is isolated and compact, making the use of dendrograms to extract source properties unnecessary. Observed properties of the centimetre emission are estimated from 2D Gaussian fitting, and are presented in Table 2. At 1.21 cm, MM1's centimetre-wavelength counterpart (here called CM1) is strongly detected ($\sim 45\sigma$), while at 5.01 cm only a $\sim 5.7\sigma$ detection is made. The fitted position of CM1 at 1.21 cm agrees well with the position of the ALMA 1.05 mm peak (within <0.″01; Table 2, Figure 2b,c). Interestingly, the 5.01 cm emission is offset to the southwest by ~0.″16 (~640 AU), ~2.4× the absolute positional uncertainty of the 5.01 cm data (estimated as 10 per cent of the geometric mean of the synthesised beam). Possible interpretations of this offset are discussed in §4.4. No centimetre emission is detected towards the other ALMA millimetre sources in our VLA 1.21 cm and 5.01 cm images, to respective 5σ limits of 30 μJy beam^{-1} and 25 μJy beam^{-1}.

3.2 Compact molecular line emission towards MM1

Our two broad spectral windows reveal a "forest" of molecular lines towards MM1. In identifying lines, we pay particular attention to those strong and unblended enough for kinematic analysis, and to typical oxygen-bearing COMs expected in hot core sources, which were conspicuously lacking in the previous SMA data (Cyganowski et al. 2011a; Section 1). We use the JPL (Pickett et al. 1998) and CDMS (Müller et al. 2001) catalogues to identify the observed molecular lines. As a number of candidate molecular lines may have indistinguishable rest frequencies within the ~1 km s^{-1} spectral resolution of the data, we produce LTE synthetic spectra for each species (e.g. Herbst & van Dishoeck 2009) using the Weeds extension (Maret et al. 2011) of the CLASS software, accounting for beam dilution. A line is considered a firm detection if the LTE synthetic spectrum reasonably reproduces the observed brightness temperatures for typical model parameters expected of a hot core, such as line rotational temperatures of > 100 K. This approach allowed the identification of some blended lines that were otherwise indistinguishable using rest frequencies alone due to our coarse spectral resolution. Using this approach, we identify 43 line transitions from 12 different species. In this paper, we focus on 19 lines from 8 species that appeared strong and unblended enough for kinematic analysis (listed in Table 3); details of other detected lines and a discussion of the chemistry of MM1 will be presented in Paper II (Williams et al. in prep.).

Figure 3 and 4a present moment one maps of the 19 lines listed in Table 3, and of the narrow-band CH_3OH (v_t=0) $11_{2,10} - 10_{3,7}$ line, respectively. Most striking is that all species show a consistent velocity gradient across MM1, with red-shifted emission to the east and blue-shifted emission to the west (with respect to the systemic velocity of 59.9 ± 1.1 km s^{-1}; Cyganowski et al. 2011a). The sense of the velocity gradient agrees with that of the 6.7 GHz Class II CH_3OH masers imaged by Cyganowski et al. (2009) (e.g. their Figure 5f). As shown in Figure 3, the extent of the compact molecular line emission is generally consistent with the measured size of MM1 from the 1.05 mm continuum emission (shown by the yellow ellipse in the bottom right panel; see also Table 2). As expected, the highest energy lines appear the most compact, with some lower energy lines appearing somewhat more extended. The three lines marked in the final column of Table 3 with "Y/N" ($H_2CO(4_{2,3} - 3_{2,1})$, CH_3OH $v_t = 0$ $(6_{1,5} - 5_{1,4})$ and $^{13}CS(6–5)$) in particular appear in Figure 3 to have more extended morphologies. On larger scales, this H_2CO and this CH_3OH line appear to trace MM1's outflow. To avoid con-

Table 3. Properties of the nineteen spectral lines identified towards MM1 for kinematic analysis in the broad ALMA spectral windows. Arranged by decreasing E_u/k_B.

Species	Transition	Frequency (GHz)	E_u/k_B (K)	σ^a (mJy beam^{-1})	Catalogue^b	Kinematics?^{c}
CH_3OH (v_t = 0)	$23_{4,19}$–$22_{5,18}$	278.96513	736.0	3.5	JPL	Y
CH_3OH (v_t = 0)	$21_{-2,20}$–$20_{-3,18}$	278.48023	563.2	3.6	JPL	Y
CH_3OH (v_t = 0)^d	$17_{6,12}$–$18_{4,13}$--	291.90814	548.6	4.2	JPL	Y
CH_3OH (v_t = 0)	$18_{5,13}$–$19_{4,16}$--	278.72314	534.6	3.5	JPL	Y
CH_3OH (v_t = 1)	$10_{1,10}$–$9_{0,9}$	292.51744	418.8	4.1	JPL	Y
CH_3OH (v_t = 0)	$14_{4,10}$–$15_{3,12}$	278.59908	339.6	3.5	JPL	Y
CH_3CH_2CN (v = 0)^e	$31_{7,24}$–$30_{7,23}$	278.00758	267.8	3.7	JPL	Y
CH_3CH_2CN (v = 0)	$31_{6,25}$–$30_{6,24}$	278.26670	253.4	3.7	JPL	Y
g-CH_3CH_2OH ^{f}	$16_{6,10}$–$15_{6,9}$ (v_t=0-0)	277.41431	213.8	3.6	JPL	Y
g-CH_3CH_2OH	$16_{4,12}$–$15_{4,11}$ (v_t=0-0)	278.64299	189.7	3.6	JPL	Y
CH_3OCH_3 ^{g}	$16_{1,16}$–$15_{0,15}$ (EA)	292.41225	120.3	4.1	JPL	Y
NH_2CHO	$13_{3,10}$–$12_{3,9}$	277.51403	119.8	3.5	JPL	Y
CH_3OCH_3 ^{h}	$13_{2,12}$–$12_{1,11}$ (EE)	291.44307	88.0	4.1	JPL	Y
H_2CO ^{i}	$4_{2,2}$–$3_{2,1}$	291.94807	82.1	4.5	CDMS	Y/N
CH_3OCH_3 ^{j}	$12_{2,11}$–$11_{1,10}$ (EE)	278.40706	76.3	3.7	JPL	Y
CH_3OH (v_t = 0) ^{i}	$6_{1,5}$–$5_{1,4}$ --	292.67291	63.7	4.1	JPL	Y/N
$^{13}CH_3OH$ (v_t = 0)	$3_{2,2}$–$4_{1,3}$	291.53662	51.4	4.1	CDMS	Y
^{13}CS (v = 0)	6–5	277.45540	46.6	3.7	CDMS	Y/N
CH_3OH (v_t = 0)	$2_{-2,1}$–$3_{-1,3}$	278.34222	32.9	3.7	JPL	Y

[a] Rms noise measured in emission-free regions of channels with complex emission.
[b] CDMS: http://www.astro.uni-koeln.de/cgi-bin/cdmssearch (Müller et al. 2001), JPL: http://spec.jpl.nasa.gov/ftp/pub/catalog/catform.html (Pickett et al. 1998)
[c] Flag marking lines used for kinematic analysis (Y) or not (Y/N). Those marked with "Y/N" appeared suitable from their isolated spectra, however exhibited extended emission.
[d] Blended with CH_3OH (v_t = 0) $17_{6,11}$–$18_{5,14}$++. Both have the same energy, JPL intensity and frequency.
[e] Blended with CH_3CH_2CN (v = 0) $31_{7,25}$–$30_{7,24}$. Both have the same energy, JPL intensity and frequency.
[f] Blended with the g-CH_3CH_2OH $16_{6,11}$–$15_{6,10}$ (v_t = 0 – 0) line, shifted from this reference transition by 0.86 km s^{-1} i.e. < 1 channel.
[g] Blended with three other CH_3OCH_3 lines with the same E_{upper}, shifted from this reference transition by 0, 0.17, 0.33 km s^{-1} i.e. < 1 channel.
[h] Blended with three other CH_3OCH_3 lines with the same E_{upper}, shifted from this reference transition by 1.55 MHz ~ 1.6 km s^{-1} i.e. < 2 channels.
[i] Outflow tracing.
[j] Blended with three other CH_3OCH_3 lines with the same E_{upper}, shifted from this reference transition by 1.7 MHz ~ 1.8 km s^{-1} i.e. < 2 channels.

tamination/confusion from larger-scale emission, we exclude these three lines from our kinematic analysis of the candidate disc.

We measure the position angle of the velocity gradient in a similar way to that outlined by Hunter et al. (2014), by measuring the slope of the line that connects the most blue-shifted and most red-shifted positions for each line. For the 16 lines in Figure 3 shown to have compact emission (excluding the 3 with more extended emission) and the narrow-band CH_3OH line in Figure 4a, we find a mean position angle of 78.0 ± 8.0° (with standard error), in agreement with the position angle of MM1 from the 1.05 mm continuum of 78.7°. We measure the position angle of the $^{12}CO(2–1)$ bipolar outflow observed by Cyganowski et al. (2011a) with the SMA to be −18.5 ± 5.0°. The position angle of the candidate disc is 96.5 ± 9.4° from that of the outflow, consistent with a perpendicular orientation and the observation of a disc-outflow system.

3.3 6.7 GHz methanol masers

Our new C-band VLA observations provide a higher-resolution view of the 6.7 GHz Class II CH_3OH maser emission associated with MM1 (imaged with 2.″8 resolution with the VLA by Cyganowski et al. 2009, §1). To characterise the morphology and kinematics of the maser emission on scales smaller than the beam, we fit the observed emission in each channel with a >5σ maser detection with a 2D Gaussian using the CASA IMFIT task. The rms noise in the maser cube is higher in channels with strong emission due to dynamic range limitations (see also §2.2); the >5σ detection criterion was applied using values of the rms noise measured for each channel within an emission-free region. The channels with >5σ maser emission in our data range in velocity from 53.7 – 63.0 km s^{-1} inclusive, and have minimum, maximum and median rms noise values of 1.89, 5.35, and 1.98 mJy beam^{-1}. The minimum fitted signal-to-noise is ~ 7.5σ (corresponding to T_B =1051 K). The masers were fit as point sources, i.e. with the major and minor axes and position angle of the emission fixed to those of the synthesised beam (see Section 2.2), as we expect the emission to be unresolved (e.g. Hunter et al. 2018; Towner et al. 2021). The fitted positions are plotted in Figure 2c and Figure 4 and tabulated in Table 4 along with the fitted peak intensities and statistical uncertainties.

As shown in Figure 2c, the 6.7 GHz masers extend over >0.″1 and coincide with the brightest 1.05 mm and 1.21 cm emission. This can also be seen in Figure 4a and in the zoom view shown in Figure 4b, which presents the fitted maser positions colour-coded by velocity. The sense of the velocity gradient seen in the masers is consistent

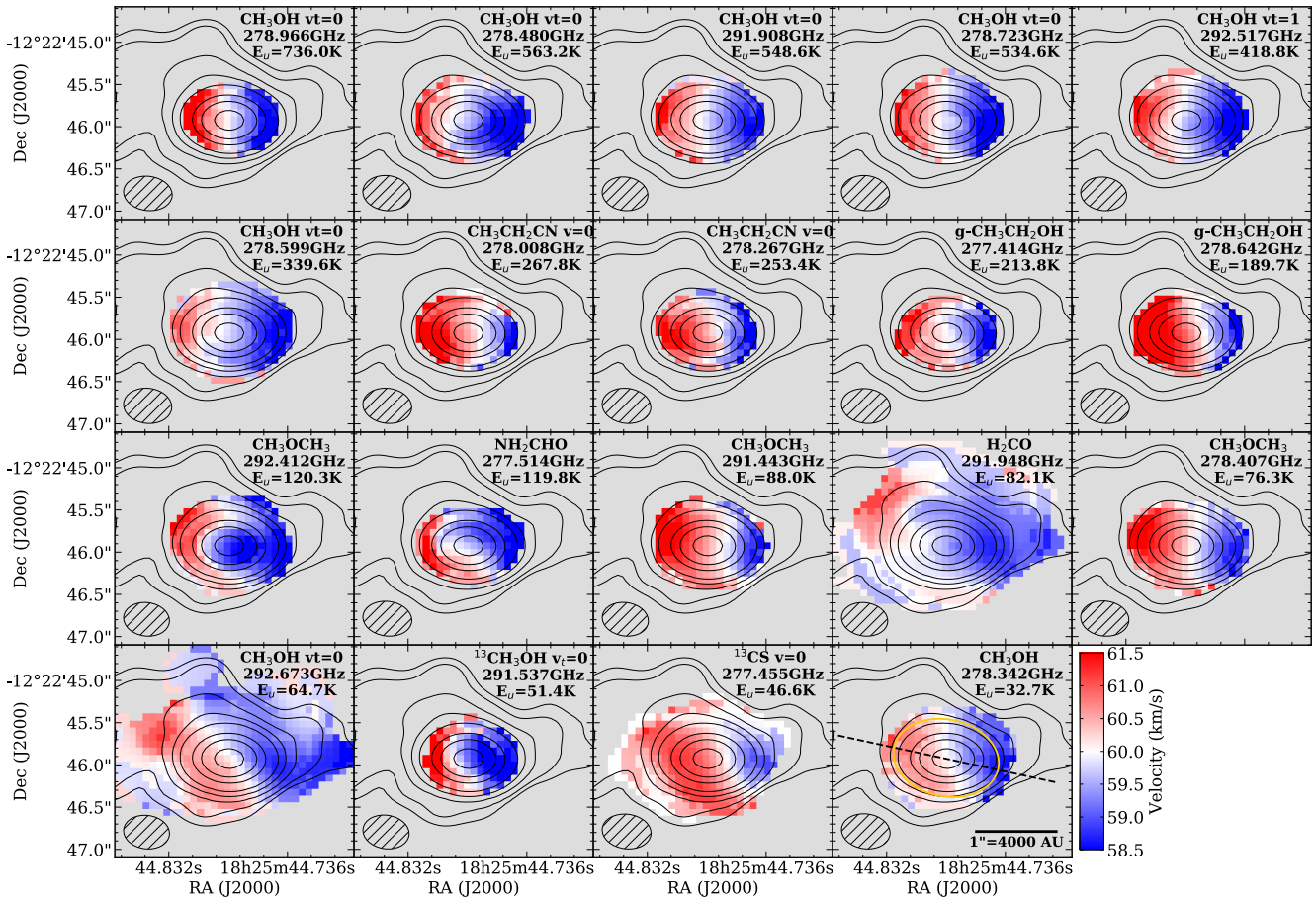


Figure 3. Moment one maps of the 19 lines in the wide ALMA spws that appeared unblended and strong enough for kinematic analysis (Table 3), arranged from top-left by decreasing upper level energy in Kelvin. Each panel is annotated with the species name, rest frequency, and upper level energy. Masked pixels (line emission $<5\sigma_{\rm median}$, where $\sigma_{\rm median}$ = 3 mJy beam^{-1} is the median rms in line-free channels from Table 1) are shown in grey. ALMA 1.05 mm continuum contours are shown in black (levels: 5, 8, 16, 32, 64, 200, 400 and 800σ). In the bottom right panel, the yellow ellipse shows the size of MM1 measured from the ALMA 1.05 mm continuum emission (Table 2), and the dashed black line shows the direction of the PV slices in Figures 6 and 7. The synthesised beam is plotted in the bottom left of each panel and a 1″ scalebar is shown in the bottom right panel.

with that of the thermal gas (Figure 4a,b): masers near the ~60 km s^{-1} systemic velocity of MM1 are near the ALMA 1.05 mm continuum peak, with blue- and red-shifted maser emission to the west and east respectively. The strongest maser emission is blueshifted (Table 4) and the intensity-weighted position for the group of masers ($18^{\rm h}25^{\rm m}44\overset{\rm s}{.}77786$ −12°22′45″.90063 (J2000)) is ~ 0″.06 ~ 240 AU from the ALMA 1.05 mm peak, as shown in Figure 4b. We note that our new intensity-weighted maser position is offset from that of Cyganowski et al. (2009) by ~ 0″.15, within the absolute positional uncertainty of the lower-resolution data estimated as 10 per cent of the geometric mean of the synthesised beam.

As illustrated by Figure 4b, our data show that the distribution of the masers forms a partial ellipse, consistent with an inclined ring, centred ~0″.04 (~160 AU) north of the 1.05 mm continuum peak. Ring-like configurations of Class II CH_3OH masers are often observed (most commonly at 6.7 GHz) and have been attributed to a range of phenomena including discs, outflows or outflow cavities and shock interfaces associated with infalling gas (e.g. Caswell 1997; De Buizer 2003; Bartkiewicz et al. 2005, 2009, 2020; Torstensson et al. 2011; Sugiyama et al. 2014, 2016; Brogan et al. 2019). An ellipse fitted to the maser positions (excluding the outlier with large uncertainties in Figure 4b) has a size of 0″.151 × 0″.072 ~ 600 × 290 AU (major × minor axis) and a position angle of ~ 80°. The position angle of the ring-like maser structure is thus consistent with those of the ALMA 1.05 mm continuum (Table 2) and the velocity gradient seen in the thermal molecular lines (§3.2), i.e. is ~perpendicular to the bipolar molecular outflow. The physical scale of the maser ring in G19.01 MM1 is similar to those of the smaller rings in the sample of Bartkiewicz et al. (2009); for comparison, the CH_3OH maser ring in the prototypical source G23.657−0.127 has a radius of 405 AU (Bartkiewicz et al. 2020). Multi-epoch VLBI imaging has shown that the motions of the G23.657−0.127 masers are dominated by radial expansion (Bartkiewicz et al. 2020), and that a combination of expansion and rotation is required to explain the motions of the 6.7 GHz CH_3OH masers in the EGO G23.01−0.41 (which are more widely distributed within an area of ~2800×2800 AU; Sanna et al. 2010). In G19.01 MM1, the consistency in velocity gradient (Figure 4a,b) and position angle between the masers and the thermal line emission suggests a rotational component to the maser motions. Masers with such motions could plausibly be associated with a (rotating) wide-angle wind at the base of a protostellar jet or the interaction of a wind with the inner regions of the disc (similar to the scenarios proposed for G23.657 and G23.01 by Bartkiewicz et al. 2020; Sanna et al. 2010, respectively), or potentially with an infall/disc interface

Table 4. Fitted properties of 6.7 GHz Class II CH_3OH maser emission.

J2000.0 Coordinates				I^b	$dI^{a,b}$	Velocity
α ($^{\rm hms}$)	dx^a ($''$)	δ ($^\circ$ $'$ $''$)	dy^a ($''$)	(Jy beam^{-1})	(Jy beam^{-1})	(km s^{-1})
18:25:44.77664	0.00165	-12:22:45.88615	0.00046	0.6413	0.0016	53.7
18:25:44.77665	0.00083	-12:22:45.88676	0.00023	1.5056	0.0019	54.0
18:25:44.77677	0.00690	-12:22:45.88037	0.00221	0.3444	0.0036	54.3
18:25:44.77784	0.00021	-12:22:45.90216	0.00006	6.5662	0.0021	54.6
18:25:44.77778	0.00017	-12:22:45.90104	0.00005	18.657	0.0046	54.9
18:25:44.77757	0.00010	-12:22:45.89795	0.00003	21.4148	0.0033	55.2
18:25:44.77755	0.00010	-12:22:45.89881	0.00003	17.1632	0.0025	55.5
18:25:44.77701	0.00011	-12:22:45.89424	0.00003	13.9754	0.0024	55.8
18:25:44.77656	0.00012	-12:22:45.89104	0.00003	14.7786	0.0026	56.1
18:25:44.77681	0.00015	-12:22:45.90387	0.00004	11.7347	0.0026	56.4

[a] Statistical uncertainties from the Gaussian fitting.
[b] T_B(K) $\approx 74551 \times I$(Jy beam^{-1})
(Only the first ten rows of this table are shown. The full table is available in a machine-readable form in the online journal.)

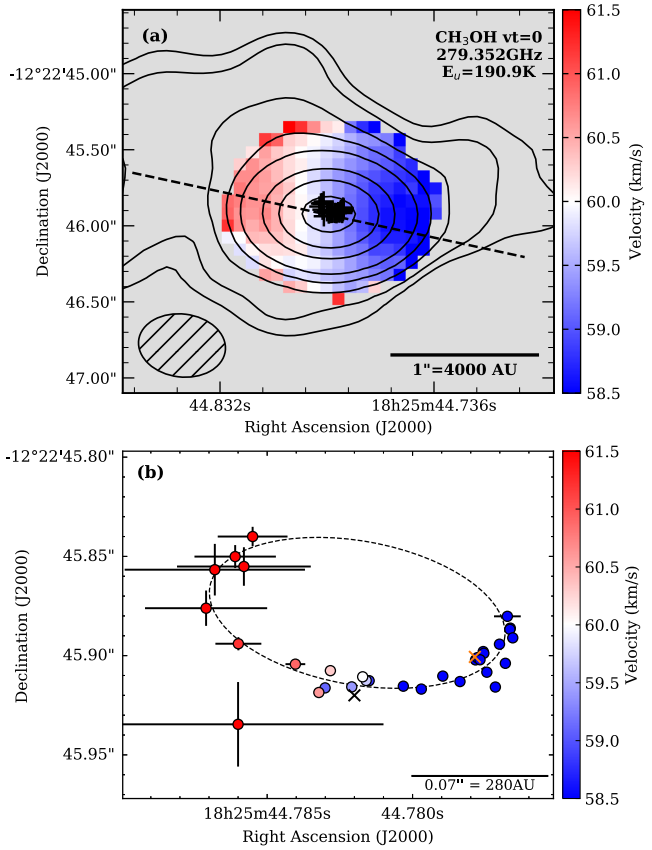


Figure 4. (a) Moment one map of the CH_3OH (v_t=0) $11_{2,10} - 10_{3,7}$ line ($\nu_{\rm rest}$ =279.35189 GHz, E_u/k_B=190.9 K) overlaid with ALMA 1.05 mm continuum contours (black) as in Figure 3. Masked pixels (line emission $<5\sigma$, where σ = 7.0 mJy beam^{-1} is the rms measured in line-free channels) are shown in grey. Black + mark the positions of 6.7 GHz Class II CH_3OH masers from Table 4. The dashed line shows the direction of the PV slice in Figure 7. The synthesised beam is plotted at bottom left, and a 1$''$ scalebar is plotted at bottom right. (b) Zoom view showing the fitted positions, with uncertainties, of the masers from Table 4, colour-coded by velocity. The black and orange × mark the ALMA 1.05 mm peak from Table 2 and the intensity-weighted maser position respectively. The fitted ellipse discussed in §3.3 is shown as a dashed black line. An 0.07$''$ scalebar is plotted at bottom right.

(as suggested for Cepheus A HW2 by Torstensson et al. 2011). Multi-epoch high-resolution observations of the 6.7 GHz masers in G19.01 MM1 would be required to establish the relative contributions of rotation and expansion or infall to the 3D maser motions to help distinguish among these scenarios.

4 DISCUSSION

4.1 Kinematic Modelling of MM1

To constrain the enclosed mass, $M_{\rm enc}$, within the candidate disc, we produce theoretical position-velocity (PV) diagrams that delineate where emission is expected for a thin circumstellar disc in Keplerian rotation and freefall onto the central mass. Following Cesaroni et al. (2011), this is expressed as:

$$V = {\rm V_{sys}} + \sin i \times \left(\sqrt{GM_{\rm enc}} \frac{x}{R^{3/2}} + \sqrt{2GM_{\rm enc}} \frac{z}{R^{3/2}} \right), \quad (1)$$

where V is the velocity along the line of sight, $V_{\rm sys}$ is the source systemic velocity, i is the line-of-sight inclination angle (where $i = 0^\circ$ corresponds to a face-on disc), $M_{\rm enc}$ is the enclosed mass, x and z are respectively co-ordinates along the plane of the disc and the line of sight, and $R = \sqrt{x^2 + z^2}$ is the distance from the centre of the disc and is limited to be between $R_{\rm in}$ (the inner radius of the disc) and $R_{\rm out}$ (the outer radius of the disc). The first term in the brackets of equation 1 corresponds to the Keplerian disc and the second term to the freefall component, interpreted as infall.

As seen in equation 1, there is a well-known degeneracy between the enclosed mass and disc inclination angle. For a given R, and pure Keplerian motions or fixed x and z, this degeneracy has the form $V - V_{\rm sys} \sim \sin i \sqrt{M_{\rm enc}}$. For the case of combined Keplerian rotation and infall, the degeneracy is illustrated by Figure 5, where (for example) models with $i = 40^\circ$ and $M_{\rm enc} = 40\,M_\odot$, $i = 50^\circ$ and $M_{\rm enc} = 30\,M_\odot$ and $i = 70^\circ$ and $M_{\rm enc} = 20\,M_\odot$ all delineate similar regions in PV space. To constrain i, we fit a 2D Gaussian to the moment zero map of each molecular line in Figure 3 with compact emission (excluding the 3 with more extended emission, §3.2, Table 3), and the narrow-band CH_3OH (v_t=0) $11_{2,10} - 10_{3,7}$ line in Figure 4a, and calculate i from the deconvolved major and minor axes assuming circular symmetry. The inclination angles calculated for these 17 lines range from i = 19 – 64°, with a median of $i = 38^\circ$ and a standard deviation of 10°. If one considered this range to be a reflection of the uncertainty in i, then

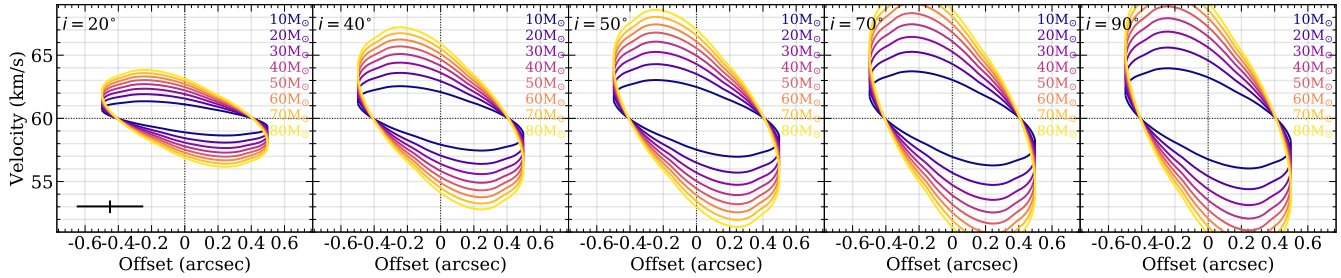


Figure 5. Position-velocity (PV) models for a thin Keplerian disc and free-fall motions (equation 1) for M_{enc} of 10–80 $M_\odot$ and disc inclination angles (i) of 20, 40, 50, 70 and 90° (from left to right, colours as labelled). In all panels, R_{out} and R_{in} are fixed to 2000 AU and 1700 AU respectively. Dotted black lines mark the systemic velocity (60 km s^{-1}) and the position of the millimetre continuum peak (zero positional offset). The angular (∼0.4″) and spectral (1.0 km s^{-1}) resolution are shown in the leftmost panel.

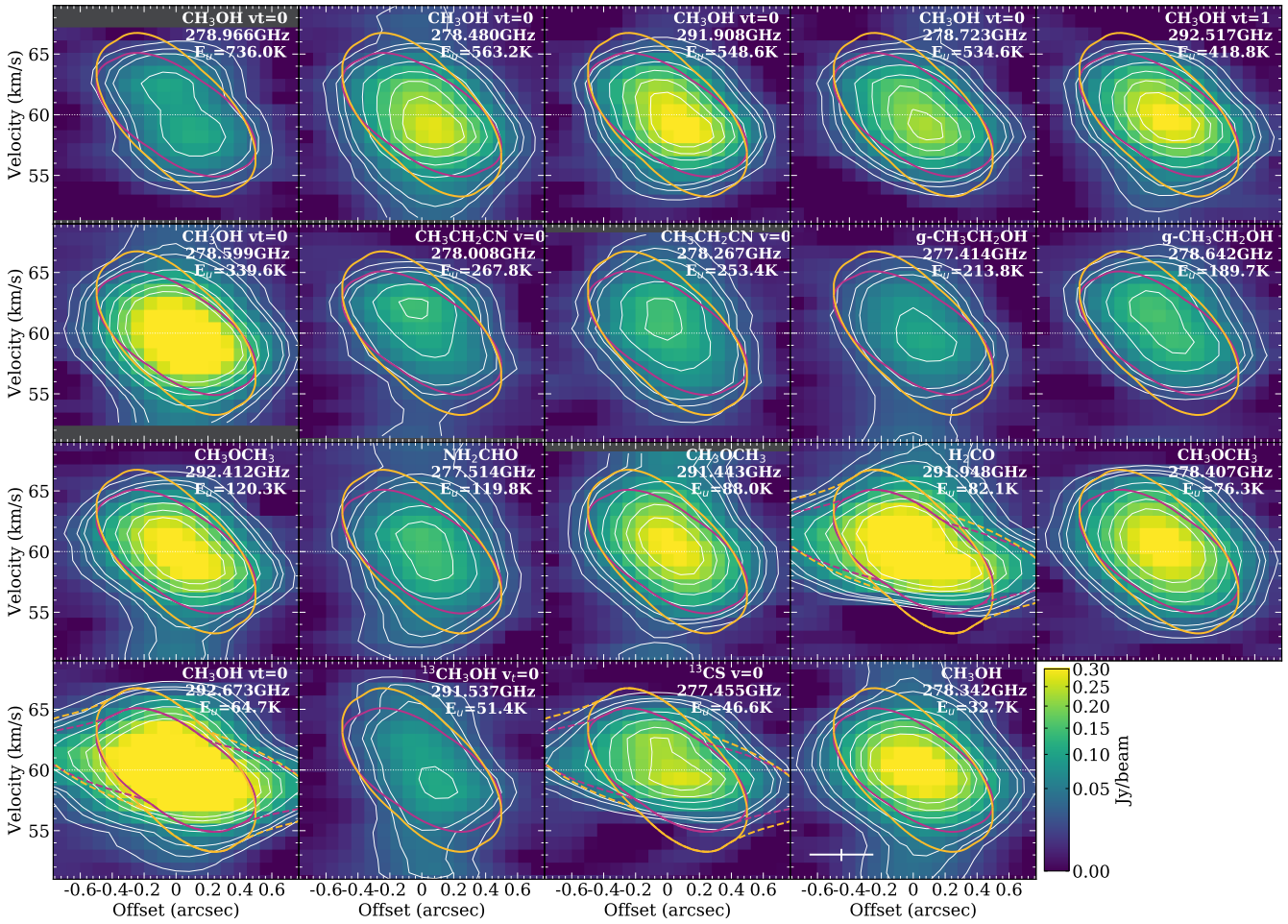


Figure 6. Position-velocity (PV) diagrams of MM1 for the 19 lines in the wide ALMA spws selected for kinematic analysis (Table 3), along a slice perpendicular to the direction of the bipolar outflow (see Figure 3). The molecule name, rest frequency, and upper energy of the transition are labelled in each panel; panels are arranged from top-left by decreasing upper level energy. White contours are plotted at 5, 9, 12, 24, 36, 48 and 60σ for each line, using the values of σ presented in Table 3. Dark grey pixels (in some panels) indicate regions of PV space outside the imaged sub-cube. PV models (equation 1) are overplotted as solid lines for i = 40°, R_{out} = 2000 AU, R_{in} = 1700 AU and M_{enc} = 40 $M_\odot$ (purple) and M_{enc} = 70 $M_\odot$ (orange), representing the range of M_{enc} that provides a reasonable match to our observed data (§4.1). For the three transitions with extended emission, the coloured dashed lines represent the same model as the corresponding solid line but with a larger R_{out} = 3500 AU. The angular (∼0.4″) and spectral (1.0 km s^{-1}) resolution are shown in the bottom right panel. The horizontal dotted white line marks the source systemic velocity of 60 km s^{-1}.

it would correspond to a factor of $(\sin i)^2 \sim 7.6$ in the mass estimate. We caution, however, that the broad range of inclinations estimated from different molecular species may be influenced by molecular abundance, chemistry, optical depth, and/or temperature effects. The equivalent calculation for i using the deconvolved 1.05 mm source size from Table 2 yields $i = 43°$ for the dust emission, in reasonable agreement with the median value of 38° from the lines. While maser-emitting rings are not necessarily co-planar with the thermal gas in the disc (e.g. Sugiyama et al. 2016), we note that the inclination angle of the maser ring, calculated from the fitted size of the ellipse (§3.3) assuming circular symmetry, is $i = 61°$, within the range found for the thermal lines. Importantly, an intermediate disc inclination angle is also consistent with the observed velocity and morphology of the bipolar molecular outflow driven by MM1 (Cyganowski et al. 2011a, see also Figure 1).

To identify the subset of PV models that provide a reasonable representation of our data, we employ a by-eye approach similar to that of Maud et al. (2018, 2019) and Ilee et al. (2018). As our primary aim is to constrain the enclosed (and so the stellar) mass, we fix R_{out} to 2000 AU based on the extent of the 1.05 mm dust continuum emission (≈ 0.5× the geometric mean of the major and minor axes from Table 2), which is in reasonable agreement with the extent of the compact molecular line emission (Figure 3). We fix the inner radius to the beamsize (R_{in} =1700 AU) to avoid producing features in the model that are not probed by our observations (see e.g. Ilee et al. 2018; Jankovic et al. 2019). For a given inclination angle i, the enclosed mass M_{enc} is then the only remaining free parameter used to tune the model. We note that since we are limited to a narrow range of radii in the outer disc, the inferred M_{enc} may be an overestimate since rotation in the outer disc is expected to be super-Keplerian (e.g. Kuiper et al. 2011; Kuiper & Hosokawa 2018).

Figures 6 and 7 show observed PV diagrams for the 19 lines in the wide ALMA spws selected for kinematic analysis (Table 3) and the narrow-band CH_3OH (v_t=0) $11_{2,10} - 10_{3,7}$ line, respectively, along a slice perpendicular to the direction of the bipolar outflow (see bottom right panel of Figure 3 and Figure 4a). The overall shapes of the structures seen in these PV diagrams are generally consistent with each other, with the most notable exceptions in Figure 6 being the three lines previously identified as exhibiting more extended emission (low-excitation lines of H_2CO, CH_3OH and ^{13}CS; Table 3, §3.2). As shown in Figure 7, the much higher spectral resolution of the narrowband data (~4× better than the wide spws; §2.1) probes higher-velocity emission near the central source (i.e. at small values of the angular offset). Differences between species, and between different transitions of the same species, are seen in the extent and structure of emission in PV diagrams of disc-tracing lines in other MYSOs, due to differences in molecular abundance, excitation, and/or optical depth (e.g. NGC 6334I(N)-SMA 1b, G11.92−0.61 MM1, and AFGL 4176; Hunter et al. 2014; Ilee et al. 2016; Johnston et al. 2020, respectively). Accretion outbursts in the recent past can also affect the appearance/extent of emission of different species (e.g. Wiebe et al. 2019; Jørgensen et al. 2020, and references therein). While we see some indications of differences that may be attributable to optical depth (e.g. the double-peaked/asymmetric structure and more limited extent of the $^{13}CH_3OH$ and E_u/k_B=736.0 K CH_3OH lines in Figure 6 compared to other CH_3OH transitions), their interpretation is limited by the angular resolution of our data. Disentangling the effects of abundance, excitation, and optical depth would require well-resolved images of a range of molecular species and transitions, and hence higher-resolution (sub)millimetre observations.

Based on the independent evidence for an inclination angle of ~40° from the dust continuum and line emission, we focused on the

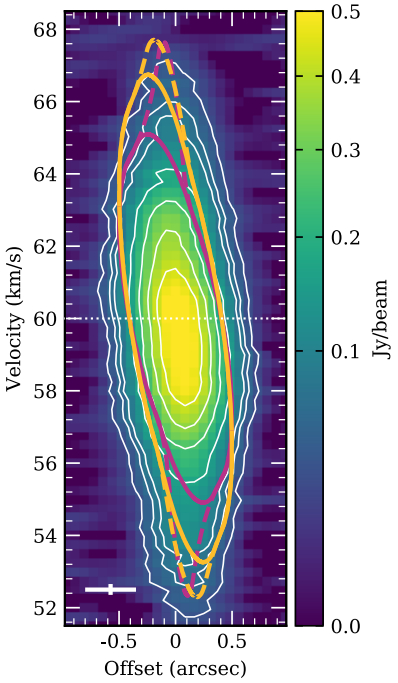


Figure 7. Position-velocity (PV) diagram of the CH_3OH (v_t=0) $11_{2,10} - 10_{3,7}$ line (ν_{rest} =279.35189 GHz, E_u/k_B=190.9 K), imaged with Δv=0.25 km s^{-1} channels (§2.1), along a slice perpendicular to the direction of the bipolar outflow (see Figure 4a). White contours are plotted at 5, 9, 12, 24, 36, 48 and 60 σ, where σ = 7.2 mJy beam^{-1} measured for emission-free regions of line-rich channels. As in Figure 6, PV models (equation 1) are overplotted as solid lines for $i = 40°$, R_{out} = 2000 AU, R_{in} = 1700 AU and M_{enc} = 40 $M_\odot$ (purple) and M_{enc} = 70 $M_\odot$ (orange). Dashed coloured lines represent models with lower values of R_{in}, of 750 AU for the 40 $M_\odot$ model (purple) and 1300 AU for the 70 $M_\odot$ model (orange). The angular (~0.4″) and spectral (0.25 km s^{-1}) resolution are shown at bottom left. The horizontal dotted white line marks the source systemic velocity of 60 km s^{-1}.

$i = 40°$ case in our exploration of M_{enc} parameter space. For $i = 40°$, and using the 5σ intensity contour to guide the eye, we found that models with enclosed masses between 40 and 70 $M_\odot$ (overplotted as coloured lines in Figures 6 and 7) provide a reasonable representation of the different shapes and extents of the observed emission of the lines along the velocity axis (the extent along the offset axis is fixed to R_{out}, marked by the intersection of the PV models with the horizontal line of the systemic velocity). Models with larger outer radii better represent the observed emission of the three lines with more extended emission (low-excitation lines of H_2CO, CH_3OH and ^{13}CS; Table 3), such as R_{out} = 3500 AU (dashed coloured lines in Figure 6). The higher-velocity emission near the central source (i.e. near offset = 0) seen in the CH_3OH line observed with higher spectral resolution (Figure 7) can be represented by models with smaller inner radii (e.g. dashed coloured lines in Figure 7) and/or higher enclosed masses, however we cannot distinguish between these parameters with the current data. We note that while higher angular resolution observations, which better resolve the candidate disc, are required to better measure i directly, we can rule out both very low and very high values of i based on the observed properties of the outflow. An edge-on or nearly edge-on disc ($i \sim 90°$) would imply an outflow in or near the plane of the sky, inconsistent with the very high-velocity ^{12}CO emission (>100 km s^{-1} from the v_{LSR}) observed by Cyganowski et al. (2011a) with the SMA. At the other extreme, a nearly face-on disc ($i \sim 0°$) is inconsistent with the extended morphology of both

the 4.5 μm emission and the high-velocity molecular gas. Thus, our kinematic modelling shows that for all plausible inclination angles, a high $M_{\rm enc}$ ($\geq$15 $M_\odot$ for $i \leq 80°$) is required to describe the observed emission. In the following sections, we adopt $M_{\rm enc} = 40 - 70\,M_\odot$, based on the range of models that best describe our data for the more probable intermediate-inclination ($i = 40°$) case.

4.2 SED modelling of MM1

In order to constrain the nature and evolutionary state of the central source, we construct and model the centimetre-millimetre wavelength spectral energy distribution (SED) of MM1. The SED, presented in Figure 8, includes our new VLA 1.21 cm and 5.01 cm and ALMA 1.05 mm data along with the SMA 1.3 mm and CARMA 3.4 mm datapoints from Cyganowski et al. (2011a). To more closely match the u,v–coverage of the VLA and ALMA data, we re-imaged the VLA 1.21 cm data with a u,v–range > $20k\lambda$. The effect of this adjustment is minimal: the resulting image has a beam size of $0\farcs32 \times 0\farcs22$ [P.A. +0.7°] and rms noise of 6.0 μ Jy beam^{-1}. For the purposes of the SED, we measure the integrated flux density at each wavelength by fitting a single 2D Gaussian to the emission, consistent with the approach of Cyganowski et al. (2011a) for the SMA and CARMA datapoints: the resulting flux densities are presented in Table 5. In Figure 8, error bars represent the statistical uncertainties from the 2D Gaussian fitting, added in quadrature with conservative estimates for the flux calibration uncertainty (5 per cent for the VLA, 10 per cent for ALMA, and 15 per cent for the SMA and CARMA).

As Figure 8 illustrates, the millimetre-wavelength emission of MM1 is dominated by dust, but dust emission alone cannot explain the observed shape of the SED. To better constrain the centimetre-wavelength portion of the SED, we imaged the VLA 5.01 cm data in two halves. These two continuum images have mean wavelengths of 6.00 cm (5.00 GHz) and 4.30 cm (6.97 GHz), synthesised beams of $1\farcs14 \times 0\farcs57$ [P.A. 73.8°] and $0\farcs83 \times 0\farcs42$ [P.A. 73.4°], and rms noise levels (1σ) of 7.8 μJy beam^{-1} and 6.4 μJy beam^{-1}, respectively. The fitted position of CM1 is $18^{\rm h}25^{\rm m}44\fs758\pm0\fs011$ $-12°22'45\farcs962\pm0\farcs064$ (J2000) in the 6.00 cm image and $18^{\rm h}25^{\rm m}44\fs7809\pm0\fs0060$ $-12°22'46\farcs0118\pm0\farcs0418$ (J2000) in the 4.30 cm image (see discussion in §4.4). The flux densities measured from these images are presented in Table 5 and Figure 8: the signal to noise of CM1 is $\sim 3.7\sigma$ in the 6.00 cm image and $\sim 5.8\sigma$ at 4.30 cm. The centimetre-wavelength spectral index calculated from these datapoints, $\alpha_{\rm 6.00cm-4.30cm} = 1.5 \pm 1.1$ ($S_\nu \propto \nu^\alpha$), is consistent with moderately optically thick free-free emission from a hypercompact (HC) H II region or ionised jet (e.g. Moscadelli et al. 2016; Purser et al. 2016; Yang et al. 2019).

We thus model MM1's centimetre-millimetre wavelength SED using a two component model (similar to the approach of Hunter et al. 2014; Brogan et al. 2016; Ilee et al. 2016), where the dust emission is described by a single-temperature modified greybody function (e.g. Gordon 1995; Rathborne et al. 2010), and the free-free emission by a Bremsstrahlung model (Olnon 1975) interpreted as an HC H II region. Since the centimetre source is marginally resolved at best, the only geometry we model is that of a uniform sphere. This combined model has seven free parameters: the electron density (n_e), radius (R_e), and electron temperature (T_e) of the HC H II region, and the angular diameter (θ_d), temperature (T_d), grain emissivity index (β), and reference opacity ($\tau_{1.3\rm mm}$) of the dust emission. Since we have only six independent datapoints, we employ a two-stage process to explore the parameter space of the combined model: 1) for each point in a grid of R_e and n_e, we fit for the five remaining free parameters; 2) adopting the best-fit H II region parameters from step 1 (based on the reduced χ^2), we fit for the dust opacity and angular diameter for each point in a grid of β and dust temperature. The best-fitting model, shown in Figure 8, has an H II region radius R_e=33 AU (consistent with the radius upper limits of 36 AU and 40 AU from Cyganowski et al. 2011b), an electron temperature of 9700 K, and an electron density of 8.6×10^5 cm^{-3}; the dust component is optically thick at millimetre wavelengths ($\tau_{1.3\rm mm}$=7), with a diameter of 1140 AU, β=2.0, and T_d=69 K. We note that this model is not unique, as there are degeneracies between model parameters that cannot be broken without additional high-resolution data: in particular, the dust temperature T_d is effectively unconstrained. By including the SMA 1.3 mm and CARMA 3.4 mm data, we are, however, able to obtain a

Table 5. Integrated continuum flux densities evaluated from 2D Gaussian fitting, and used in the SED fit.

Wavelength	Frequency (GHz)	Flux density[a] (mJy)	Imaged u,v–coverage[b] (kλ)
6.00 cm[c]	5.00	0.028 ± 0.007	20 – 276
5.01 cm[d]	5.99	0.038 ± 0.011	20 – 330
4.30 cm	6.97	0.046 ± 0.013	20 – 385
1.21 cm	24.81	0.296 ± 0.011	20 – 825
3.4 mm[e]	88.0	27 ± 3	1.5 – 36.5
1.3 mm[e]	225.1	275 ± 7	7 – 88
1.05 mm	285.12	313.1 ± 0.5	19 – 508

[a] Uncertainties are the statistical uncertainties from the Gaussian fitting.
[b] Projected baseline ranges used in the images used to construct the SED, including the adjustments described in §2.2 and §4.2.
[c] Source size fixed to the synthesised beamsize for fitting due to low S/N (~3.7).
[d] From Table 2: this point is plotted in Figure 8 but not included in the SED fit, due to the inclusion of the 4.30 cm and 6.00 cm flux densities (see §4.2).
[e] From Cyganowski et al. (2011a)

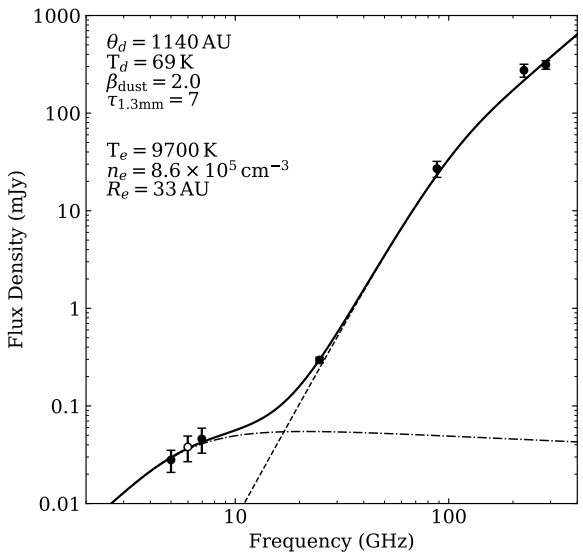


Figure 8. Spectral energy distribution of MM1 from cm to mm wavelengths. Points plotted in black are used for fitting; the 5.01 cm flux density is overplotted for reference but does not contribute to the fit (Table 5, §4.2). Plotted error bars include the statistical uncertainties from Table 5 added in quadrature with the flux calibration uncertainty (see §4.2). The best-fitting combined model is overplotted as a solid black line, with the dust component shown as a dashed line and the free-free component as a dot-dashed line. The parameters of the best-fitting model are printed at upper left.

good constraint on β, which is important for constraining the relative contributions of the dust and free-free components at intermediate frequencies. In sum, our modelling demonstrates that emission from both dust and ionised gas is required to explain the observed SED of MM1. Our results support a picture in which the ionised gas is confined to a very small HC H II region, suggesting that the H II region may be gravitationally "trapped" by an accretion flow (e.g. Keto 2003, 2007), consistent with other evidence for ongoing accretion (§1).

4.3 Disc properties and stability

Our SED modelling confirms that the ALMA 1.05 mm emission of MM1 is dominated by thermal dust emission, with dust accounting for 99.99% of the 1.05 mm flux density in our best-fitting model. We estimate the mass, M_{gas}, of MM1 from its 1.05 mm integrated flux density in Table 2, assuming isothermal dust emission and correcting for the dust optical depth (e.g. Cyganowski et al. 2011a, 2017):

$$M_{gas} = \frac{d^2 \, R \, S_\nu \, C_{\tau_{dust}}}{\kappa_\nu \, B_\nu(T_{dust})} , \quad (2)$$

where d is the distance, R is the gas-to-dust mass ratio (assumed to be 100), S_ν is the 1.05 mm integrated flux density, κ_ν is the dust opacity at 1.05 mm, $B_\nu(T_{dust})$ is the Planck function, T_{dust} is the dust temperature, and $C_{\tau_{dust}}$ is a correction for the dust optical depth:

$$C_{\tau_{dust}} = \tau_{dust}/(1 - e^{-\tau_{dust}}) , \quad (3)$$

where τ_{dust} is estimated as:

$$\tau_{dust} = -\ln\left(1 - \frac{T_b}{T_{dust}}\right) . \quad (4)$$

As in Cyganowski et al. (2017), we assume $\kappa_{1.05mm}$ =1.45 cm^2 g^{-1} (for grains with ice mantles in high gas density environments; Ossenkopf & Henning 1994). We estimate T_b as the mean Planck brightness temperature across the intensity-weighted second moment size of MM1 (10.9 K). On this sizescale, for temperatures T_{dust} = 100 – 130 K (based on the CH_3CN fitting in Cyganowski et al. 2011a), we calculate dust optical depths $\tau_{dust} \sim 0.09–0.12$ and a gas mass $M_{gas} \sim 5.4–7.2\,M_\odot$ for MM1. We note, however, that these estimates do not capture expected variations in temperature and opacity within a disc (e.g. Carrasco-González et al. 2019; Jankovic et al. 2019), and that our adopted temperature range may underestimate the temperature on the smaller sizescales probed by our ALMA observations.

With these caveats in mind, we can consider the stability of the star-disc system in MM1 based on the physical parameters of the star and circumstellar disc derived from our observations. The disc-to-star mass ratio (M_d/M_*) is often used as a proxy for the gravitational (in)stability of a disc, with unstable discs typically having values > 0.1 (e.g. Kratter & Lodato 2016, and references therein). Such a stability criterion relies on the evaluation of a reliable disc mass; however, simple mass estimates based on millimetre continuum emission (as in equation 2, or assuming optically thin emission) can underestimate the disc mass, as they do not account for variations in temperature, dust opacity, and dust optical depth within the disc (e.g. Johnston et al. 2015; Forgan et al. 2016). Forgan et al. (2016) computed semi-analytical disc models for five massive young stars with candidate discs from the literature, allowing a direct comparison of the "true" disc mass in each model with the observed mass that would be inferred from millimetre observations (adopting common assumptions, including optically thin emission). For this sample, which included star-disc systems broadly similar in properties to MM1, Forgan et al. (2016) found that a system with a "true" disc-to-star mass ratio of ~ 0.2, indicative of instability, could have an *observed* disc-to-star mass ratio of ≤ 0.05.

For MM1, attributing the M_{gas} estimated above to the disc and estimating the stellar mass as $M_* = M_{enc} - M_d \simeq 33–65\,M_\odot$, we find $M_d/M_* \sim 0.08 – 0.22$. At the cusp of stability (i.e. $M_d/M_* = 0.1$), and for $M_d = 5.4\,M_\odot$ (the low end of our range) to check for the most stable case, an enclosed mass of $\gtrsim 59\,M_\odot$ is required for the system to be stable. If the true disc mass is in fact higher than our observational estimate, as discussed above, this would have the effect of making the disc more unstable, in turn requiring an even larger enclosed mass for stability. We note that if the dust temperature on the sizescales probed by our ALMA observations is higher than our adopted temperature range, this would have the effect of decreasing our estimate of M_d and pushing the system towards stability. We calculate the minimum T_{dust} for which the system would be stable (for isothermal dust emission, and other assumptions as outlined above): 112 K for M_{enc} = 70 $M_\odot$ and 186 K for M_{enc} = 40 $M_\odot$. Subsequent higher-resolution studies of the other EGO studied by Cyganowski et al. (2011a), G11.92–0.61, suggest that a resolution-dependent temperature increase of ~ 60-70 K is possible: Ilee et al. (2016) found that two components with temperatures of ~150 and 230 K were required to model the CH_3CN spectra of the G11.92–0.61 MM1 disc in ~0.″5-resolution SMA observations, compared to 77 and 166 K for the ~2.″4-resolution observations of Cyganowski et al. (2011a).

On the whole, our results suggest that while the G19.01–0.03 MM1 disc could be stable, this would likely require the enclosed mass to be at the high end of our 40 – 70 $M_\odot$ range. We thus speculate that, based on our data, it is more likely that G19.01–0.03 MM1 is unstable and may be undergoing fragmentation into as-yet undetected low mass stellar companions, as seen in G11.92–0.61 MM1 (Ilee et al. 2018). To test this hypothesis, we proposed high-resolution (~0.″09~370 AU) ALMA observations. These ongoing observations will have the spatial resolution and sensitivity to map the temperature structure of the candidate disc and search for evidence of fragmentation.

4.4 The Nature of MM1

The bolometric luminosity of G19.01–0.03 MM1 is ~10^4 $L_\odot$ (based on fitting the MIR-mm wavelength SED; Cyganowski et al. 2011a).[1] This is inconsistent with the enclosed mass of 40–70 $M_\odot$ favoured by our kinematic modelling (§4.1) for the case of a single central object: if the stellar mass of $M_* = M_{enc} - M_d \simeq 33 – 65\,M_\odot$ corresponded to a single ZAMS star, the expected luminosity would be >10^5 $L_\odot$ (e.g. Davies et al. 2011, Table 1). The evidence for ongoing accretion in G19.01–0.03 MM1 (§1) means that the central source is unlikely to be in a ZAMS configuration, as discussed below. Interestingly, comparison of observed MYSOs with candidate discs in the literature (e.g. Table 7 of Johnston et al. 2020) suggests that there is not a monotonic relationship between luminosity and enclosed stellar mass (though luminosity estimates are affected by distance uncertainties, in particular for sources without maser parallax distances; see also Ilee et al. 2016). Notably, a third of the sources tabulated by Johnston et al. (2020) are EGOs: G11.92–0.61 MM1, G23.01–0.41, G328.2551–0.5321 (EGO G328.25–0.53) and IRAS 16547–4247

[1] The difference in assumed distance (4.0 kpc in this work compared to 4.2 kpc in Cyganowski et al. 2011a) corresponds to a decrease in luminosity of ~9 per cent, within the uncertainty of the Cyganowski et al. (2011a) estimate (see their Figure 18b).

(EGO G343.12−0.06) (Ilee et al. 2018; Sanna et al. 2019; Csengeri et al. 2018; Zapata et al. 2019, respectively). While this is a small subsample, we note that even when considering only EGOs – with similar MIR evidence for active outflows and so ongoing accretion – there does not appear to be a monotonic relation between luminosity and enclosed mass, with G11.92−0.61 MM1 having the lowest luminosity ($\sim10^4$ $L_\odot$, Cyganowski et al. 2011a; Moscadelli et al. 2016) and the highest stellar mass (>30 $M_\odot$, compared to ≤20$M_\odot$ for the other sources: Ilee et al. 2018; Johnston et al. 2020).

It is now well understood that, in general, accretion affects the configuration (stellar radius and effective temperature) of accreting protostars (e.g. Hosokawa & Omukai 2009; Hosokawa et al. 2010; Kuiper & Yorke 2013; Vorobyov et al. 2017). Hosokawa & Omukai (2009), Hosokawa et al. (2010), and Kuiper & Yorke (2013) consider these effects for the high rates of mass accretion expected for high mass star formation. These models show that as a protostar accretes solar masses of material, it is expected to undergo a swelling phase which causes the effective temperature to drop such that it is too low to produce an ionising flux sufficient for the creation of an H II region. Following the swelling phase, the protostar contracts and the effective temperature increases enough for ionisation. As recently shown by Meyer et al. (2019), this is expected to happen in an episodic fashion in response to accretion outbursts, with MYSOs repeatedly experiencing episodes of bloating followed by "unswelling". As discussed by Cyganowski et al. (2011b), the MIR-mm SED of G19.01−0.03 MM1 is well-fit by swollen, low-temperature models (T<5000 K), though hotter (10,000 K < T <30,000 K) models are also allowed (e.g. their Figure 6). As discussed in §4.2, the very small HC H II region implied by our SED modelling is consistent with gravitational "trapping" by an accretion flow; a swollen, non-ZAMS configuration would also contribute to the weakness of the observed centimetre-wavelength continuum emission (§3.1, §4.2).

An enclosed stellar mass of ∼33−65 $M_\odot$ corresponding to a single MYSO would place G19.01−0.03 MM1 among the most massive proto-O star candidates discovered to date. Of the handful of sources with reported central stellar masses >30 $M_\odot$ (AFGL 2591-VLA3, G11.92−0.61 MM1, G17.64+0.16, G31.41+0.31: Jiménez-Serra et al. 2012; Ilee et al. 2018; Maud et al. 2019; Beltrán et al. 2018, respectively; see also Johnston et al. 2020), only G17.64+0.16 (AFGL 2136) and AFGL 2591-VLA3 have central stellar masses ≥40 $M_\odot$ and both have luminosities $\geq10^5$ $L_\odot$. Theoretical models of accreting protostars also predict $L>10^5$ $L_\odot$ for $M_* >30$ $M_\odot$ (e.g. Figure 12 of Kuiper & Yorke 2013). This, together with the positional offset noted in §3.1, motivates the consideration of another possibility: that the central stellar mass is instead distributed in a high-mass binary system.

The presence of a binary could potentially explain the offset (of ∼0.″16 ∼640 AU; §3.1) between the peak of the thermal dust emission and the VLA 5.01 cm continuum emission. One possible interpretation of the offset 5.01 cm emission is an asymmetric H II region. In a single MYSO scenario, however, the centimetre emission from an H II region expanding into the cavities of the bipolar outflow (e.g. Sartorio et al. 2019; Kuiper & Hosokawa 2018, and references therein) would be expected to be aligned with the outflow axis, which does not appear to be the case in G19.01 (Figure 2c). The centimetre emission from an ionised jet would similarly be expected to be aligned with the bipolar outflow (e.g. Guzmán et al. 2010). Interestingly, from the VLA 4.30 and 6.00 cm images described in §4.2, there is a hint that the higher frequency (6.97 GHz/4.30 cm) emission may peak nearer the dust continuum than the lower frequency (5.00 GHz/6.00 cm) emission, as expected for collimated ionised jets (e.g. Reynolds 1986, and observations of Cepheus A HW2 by Rodriguez et al. 1994). We caution, however, that from the present data it is unclear if this is a significant result: the difference in the 4.30 and 6.00 cm positions is only ∼2.1× the uncertainty in the 6.00 cm position, and the direction of the offset – along an ∼E-W axis, with the lower frequency emission to the W – is inconsistent with expectations for an ionised jet from a single MYSO, as outlined above. In the case of a binary system, an H II region and/or ionised jet could behave as expected with respect to an unresolved neighbouring source.

In sum, our results are consistent with the observation of a Keplerian disc + infalling material, and of at least one MYSO given the high enclosed mass for all plausible inclination angles (§4.1). We note that adopting a higher (more nearly edge-on) inclination angle would reduce the inferred enclosed mass, reducing the mass-luminosity discrepancy (for the assumption of a single MYSO). Our ongoing 0.″09-resolution (∼370 AU) ALMA observations will help to illuminate the nature of MM1 by better resolving the disc and its kinematics, providing improved estimates of the disc inclination and enclosed mass. These observations will also have sufficient linear resolution to detect wide binaries, such as the low-mass companion detected by Ilee et al. (2018) in G11.92−0.61 MM1 with a separation of ∼1920 AU. Much closer binary companions are ubiquitous among O stars visible in the optical and NIR (e.g. Sana et al. 2014, who find 100 per cent of O dwarfs in their sample have a companion within 105 AU), and high-mass (proto)binaries with separations of 170 and 180 AU have recently been observed in IRAS 17216-3801 and IRAS 07299-1651 (Kraus et al. 2017; Zhang et al. 2019, respectively). Searching for a comparably tight (proto)binary at the distance of G19.01−0.03 would require observations in the most extended ALMA configurations, highlighting the importance of long-baseline millimetre interferometric observations.

5 CONCLUSIONS

In this paper (Paper I), we have presented a study of the nature and kinematics of the high mass (proto)star G19.01–0.03 MM1, using new subarcsecond-resolution ALMA 1.05 mm and VLA 1.21 cm and 5.01 cm data. Our main findings are as follows.

(i) Compact molecular line emission detected with ALMA towards the MM1 millimetre continuum source exhibits a velocity gradient that is approximately perpendicular to the high-velocity bipolar molecular outflow driven by MM1. This velocity gradient is consistently traced by 20 lines of varying excitation energies of 8 molecular species, including the complex organic molecules (COMs) CH_3OH, CH_3OCH_3, g-CH_3CH_2OH, CH_3CH_2CN, and NH_2CHO.

(ii) Kinematic modelling shows that the observed velocities are well represented by a Keplerian disc model, including infalling material, with an enclosed mass of 40 − 70 $M_\odot$ within a 2000 AU radius for an intermediate inclination angle of $i = 40°$ (estimated from the deconvolved sizes of the continuum and line emission). This places G19.01–0.03 MM1 among the most massive proto-O star candidates with Keplerian discs to date.

(iii) A centimetre-wavelength counterpart to MM1, CM1, is detected for the first time in our VLA 1.21 and 5.01 cm images. Our modelling of the centimetre-millimetre wavelength SED confirms that thermal dust emission dominates at millimetre wavelengths, while a free-free component is required to explain the centimetre-wavelength emission. The best-fit size of the ionised component (R_e=33 AU) is consistent with a small, gravitationally trapped hypercompact H II region.

(iv) Our high-resolution observations show that the 6.7 GHz Class II CH_3OH masers form a partial ellipse, consistent with an inclined

ring with a fitted size of ~600×290 AU, centred ~0.″04 (160 AU) north of the 1.05 mm continuum peak. The masers exhibit a velocity gradient consistent with that seen on larger scales in the thermal gas, suggestive of a rotational component to the maser motions.

(v) We estimate a disc gas mass of 5.4 – 7.2 $M_\odot$ (for T_{dust} =130-100 K) from the observed 1.05 mm flux density, assuming a simple model of isothermal dust emission. This implies a central stellar mass ($M_{enc}-M_{disc}$) of 33 – 65 $M_\odot$. Based on the disc-to-star mass ratio, our results indicate that the disc is likely to be unstable to fragmentation.

(vi) The bolometric luminosity of G19.01−0.03 (~10^4 $L_\odot$) is lower than expected for a single accreting MYSO or ZAMS star with a stellar mass of 33 – 65 $M_\odot$. This apparent discrepancy could be explained by multiplicity of the central source, with the mass distributed in an unresolved high-mass binary. The peak of the VLA 5.01 cm emission is offset from the ALMA 1.05 mm and VLA 1.2 cm emission peaks by 0.16″ ~ 640 AU, providing tentative evidence for a binary interpretation.

In all, our results support the picture that G19.01–0.03 MM1 is a hot core source that harbours at least one MYSO, and potentially a high-mass binary system, which excites a small HC H II region and is fed by a Keplerian disc and ongoing infall. Higher angular and spectral resolution observations are required to further constrain the kinematic properties of the disc, search for disc fragmentation, and ascertain if MM1 hosts a high-mass binary system. Our ongoing ALMA observations, which can address many of these questions, will be presented in a future paper.

ACKNOWLEDGEMENTS

We thank the referee, Rolf Kuiper, for a constructive report that helped clarify points in this manuscript. G.M.W. acknowledges support from the UK's Science and Technology Facilities Council (STFC) under ST/R000905/1 and ST/M001296/1, and wishes to thank Mark Thompson for useful discussion. C.J.C. acknowledges support from the UK's STFC under ST/M001296/1 and J.D.I. acknowledges support from the UK's STFC under ST/T000287/1. J.M.D.K gratefully acknowledges funding from the Deutsche Forschungsgemeinschaft (DFG, German Research Foundation) through an Emmy Noether Research Group (grant number KR4801/1-1) and the DFG Sachbeihilfe (grant number KR4801/2-1), as well as from the European Research Council (ERC) under the European Union's Horizon 2020 research and innovation programme via the ERC Starting Grant MUSTANG (grant agreement number 714907). This research has made use of: NASA's Astrophysics Data System Bibliographic Services, GILDAS (https://www.iram.fr/IRAMFR/GILDAS) and Python packages Astropy (Astropy Collaboration et al. 2013), astrodendro (Rosolowsky et al. 2008), APLPY (http://aplpy.github.com), cmocean (Thyng et al. 2016), Matplotlib (Hunter 2007), NumPy (Harris et al. 2020), pandas (McKinney 2010) and scitkit-image (van der Walt et al. 2014). This paper makes use of the following ALMA data: ADS/JAO.ALMA#2013.1.00812.S. ALMA is a partnership of ESO (representing its member states), NSF (USA) and NINS (Japan), together with NRC (Canada), NSC and ASIAA (Taiwan), and KASI (Republic of Korea), in cooperation with the Republic of Chile. The Joint ALMA Observatory is operated by ESO, AUI/NRAO and NAOJ. The National Radio Astronomy Observatory is a facility of the National Science Foundation operated under cooperative agreement by Associated Universities, Inc.

DATA AVAILABILITY

The data underlying this article will be shared on reasonable request to the corresponding author.

REFERENCES

Añez-López N., et al., 2020, ApJ, 888, 41
Astropy Collaboration et al., 2013, A&A, 558, A33
Bartkiewicz A., Szymczak M., van Langevelde H. J., 2005, A&A, 442, L61
Bartkiewicz A., Szymczak M., van Langevelde H. J., Richards A. M. S., Pihlström Y. M., 2009, A&A, 502, 155
Bartkiewicz A., Sanna A., Szymczak M., Moscadelli L., van Langevelde H. J., Wolak P., 2020, A&A, 637, A15
Beltrán M. T., de Wit W. J., 2016, A&ARv, 24, 6
Beltrán M. T., et al., 2014, A&A, 571, A52
Beltrán M. T., et al., 2018, A&A, 615, A141
Benjamin R. A., et al., 2003, PASP, 115, 953
Beuther H., Schilke P., Gueth F., McCaughrean M., Andersen M., Sridharan T. K., Menten K. M., 2002, A&A, 387, 931
Billington S. J., et al., 2019, MNRAS, 490, 2779
Brogan C. L., Hunter T. R., Cyganowski C. J., Friesen R. K., Chandler C. J., Indebetouw R., 2011, ApJ, 739, L16
Brogan C. L., Hunter T. R., Cyganowski C. J., Chandler C. J., Friesen R., Indebetouw R., 2016, ApJ, 832, 187
Brogan C. L., et al., 2019, ApJ, 881, L39
Carrasco-González C., et al., 2019, ApJ, 883, 71
Caswell J. L., 1997, MNRAS, 289, 203
Cesaroni R., Galli D., Lodato G., Walmsley C. M., Zhang Q., 2007, in Protostars and Planets V. p. 197 (arXiv:astro-ph/0603093)
Cesaroni R., Beltrán M. T., Zhang Q., Beuther H., Fallscheer C., 2011, A&A, 533, A73
Cesaroni R., Galli D., Neri R., Walmsley C. M., 2014, A&A, 566, A73
Cesaroni R., et al., 2017, A&A, 602, A59
Chevance M., et al., 2020, MNRAS, 493, 2872
Churchwell E., et al., 2009, PASP, 121, 213
Cragg D. M., Sobolev A. M., Godfrey P. D., 2005, MNRAS, 360, 533
Csengeri T., et al., 2018, A&A, 617, A89
Cyganowski C. J., et al., 2008, AJ, 136, 2391
Cyganowski C. J., Brogan C. L., Hunter T. R., Churchwell E., 2009, ApJ, 702, 1615
Cyganowski C. J., Brogan C. L., Hunter T. R., Churchwell E., Zhang Q., 2011a, ApJ, 729, 124
Cyganowski C. J., Brogan C. L., Hunter T. R., Churchwell E., 2011b, ApJ, 743, 56
Cyganowski C. J., Koda J., Rosolowsky E., Towers S., Donovan Meyer J., Egusa F., Momose R., Robitaille T. P., 2013, ApJ, 764, 61
Cyganowski C. J., Brogan C. L., Hunter T. R., Smith R., Kruijssen J. M. D., Bonnell I. A., Zhang Q., 2017, MNRAS, 468, 3694
Davies B., Hoare M. G., Lumsden S. L., Hosokawa T., Oudmaijer R. D., Urquhart J. S., Mottram J. C., Stead J., 2011, MNRAS, 416, 972
De Buizer J. M., 2003, MNRAS, 341, 277
Forgan D. H., Ilee J. D., Cyganowski C. J., Brogan C. L., Hunter T. R., 2016, MNRAS, 463, 957
Friesen R. K., Bourke T. L., Di Francesco J., Gutermuth R., Myers P. C., 2016, ApJ, 833, 204
Girart J. M., et al., 2017, ApJ, 847, 58
Goodman A. A., Rosolowsky E. W., Borkin M. A., Foster J. B., Halle M., Kauffmann J., Pineda J. E., 2009, Nature, 457, 63
Gordon M. A., 1995, A&A, 301, 853
Guzmán A. E., Garay G., Brooks K. J., 2010, ApJ, 725, 734
Harris C. R., et al., 2020, arXiv e-prints, p. arXiv:2006.10256
Herbst E., van Dishoeck E. F., 2009, ARA&A, 47, 427
Hosokawa T., Omukai K., 2009, ApJ, 691, 823
Hosokawa T., Yorke H. W., Omukai K., 2010, ApJ, 721, 478
Hunter J. D., 2007, Computing in Science and Engineering, 9, 90

Hunter T. R., Brogan C. L., Cyganowski C. J., Young K. H., 2014, ApJ, 788, 187
Hunter T. R., et al., 2018, ApJ, 854, 170
Ilee J. D., Cyganowski C. J., Nazari P., Hunter T. R., Brogan C. L., Forgan D. H., Zhang Q., 2016, MNRAS, 462, 4386
Ilee J. D., Cyganowski C. J., Brogan C. L., Hunter T. R., Forgan D. H., Haworth T. J., Clarke C. J., Harries T. J., 2018, ApJ, 869, L24
Jankovic M. R., et al., 2019, MNRAS, 482, 4673
Jiménez-Serra I., Zhang Q., Viti S., Martín-Pintado J., de Wit W. J., 2012, ApJ, 753, 34
Jiménez-Serra I., Báez-Rubio A., Martín-Pintado J., Zhang Q., Rivilla V. M., 2020, ApJ, 897, L33
Johnston K. G., et al., 2015, ApJ, 813, L19
Johnston K. G., Hoare M. G., Beuther H., Linz H., Boley P., Kuiper R., Kee N. D., Robitaille T. P., 2020, ApJ, 896, 35
Jones B. M., et al., 2020, MNRAS, 493, 2015
Jørgensen J. K., Belloche A., Garrod R. T., 2020, ARA&A, 58, 727
Kauffmann J., Pillai T., Zhang Q., Menten K. M., Goldsmith P. F., Lu X., Guzmán A. E., Schmiedeke A., 2017, A&A, 603, A90
Keto E., 2003, ApJ, 599, 1196
Keto E., 2007, ApJ, 666, 976
Kim J., et al., 2020, arXiv e-prints, p. arXiv:2012.00019
Klassen M., Pudritz R. E., Kuiper R., Peters T., Banerjee R., 2016, ApJ, 823, 28
Kratter K., Lodato G., 2016, ARA&A, 54, 271
Kraus S., et al., 2017, ApJ, 835, L5
Kruijssen J. M. D., et al., 2019, Nature, 569, 519
Krumholz M. R., Klein R. I., McKee C. F., Offner S. S. R., Cunningham A. J., 2009, Science, 323, 754
Kuiper R., Hosokawa T., 2018, A&A, 616, A101
Kuiper R., Yorke H. W., 2013, ApJ, 772, 61
Kuiper R., Klahr H., Beuther H., Henning T., 2011, ApJ, 732, 20
Lu X., Cheng Y., Ginsburg A., Longmore S. N., Kruijssen J. M. D., Battersby C., Zhang Q., Walker D. L., 2020, ApJ, 894, L14
Maret S., Hily-Blant P., Pety J., Bardeau S., Reynier E., 2011, A&A, 526, A47
Maud L. T., et al., 2018, A&A, 620, A31
Maud L. T., et al., 2019, A&A, 627, L6
McKinney W., 2010, in Stéfan van der Walt & Jarrod Millman ed., Proceedings of the 9th Python in Science Conference. pp 56 – 61, doi:10.25080/Majora-92bf1922-00a
Meyer D. M. A., Kuiper R., Kley W., Johnston K. G., Vorobyov E., 2018, MNRAS, 473, 3615
Meyer D. M. A., Haemmerlé L., Vorobyov E. I., 2019, MNRAS, 484, 2482
Mignon-Risse R., González M., Commerçon B., Rosdahl J., 2021, arXiv e-prints, p. arXiv:2105.14543
Moscadelli L., et al., 2016, A&A, 585, A71
Mottram J. C., et al., 2011, ApJ, 730, L33
Müller H. S. P., Thorwirth S., Roth D. A., Winnewisser G., 2001, A&A, 370, L49
Olnon F. M., 1975, A&A, 39, 217
Ossenkopf V., Henning T., 1994, A&A, 291, 943
Pickett H. M., Poynter R. L., Cohen E. A., Delitsky M. L., Pearson J. C., Müller H. S. P., 1998, J. Quant. Spectrosc. Radiative Transfer, 60, 883
Purser S. J. D., et al., 2016, MNRAS, 460, 1039
Rathborne J. M., Jackson J. M., Chambers E. T., Stojimirovic I., Simon R., Shipman R., Frieswijk W., 2010, ApJ, 715, 310
Reid M. J., et al., 2014, ApJ, 783, 130
Reynolds S. P., 1986, ApJ, 304, 713
Rigby A. J., et al., 2018, A&A, 615, A18
Rodriguez L. F., Garay G., Curiel S., Ramirez S., Torrelles J. M., Gomez Y., Velazquez A., 1994, ApJ, 430, L65
Rosen A. L., Krumholz M. R., McKee C. F., Klein R. I., 2016, MNRAS, 463, 2553
Rosen A. L., Li P. S., Zhang Q., Burkhart B., 2019, ApJ, 887, 108
Rosolowsky E. W., Pineda J. E., Kauffmann J., Goodman A. A., 2008, ApJ, 679, 1338
Rosolowsky E., et al., 2010, ApJS, 188, 123
Sana H., et al., 2014, ApJS, 215, 15
Sánchez-Monge Á., et al., 2013, A&A, 552, L10
Sanna A., Moscadelli L., Cesaroni R., Tarchi A., Furuya R. S., Goddi C., 2010, A&A, 517, A78
Sanna A., et al., 2019, A&A, 623, A77
Sartorio N. S., Vandenbroucke B., Falceta-Goncalves D., Wood K., Keto E., 2019, MNRAS, 486, 5171
Schuller F., et al., 2009, A&A, 504, 415
Sugiyama K., et al., 2014, A&A, 562, A82
Sugiyama K., et al., 2016, PASJ, 68, 72
Thyng K. M., Greene C. A., Hetland R. D., Zimmerle H. M., DiMarco S. F., 2016, Oceanography, 29, 3
Torstensson K. J. E., van Langevelde H. J., Vlemmings W. H. T., Bourke S., 2011, A&A, 526, A38
Towner A. P. M., Brogan C. L., Hunter T. R., Cyganowski C. J., McGuire B. A., Indebetouw R., Friesen R. K., Chandler C. J., 2017, ApJS, 230, 22
Towner A. P. M., Brogan C. L., Hunter T. R., Cyganowski C. J., 2021, arXiv e-prints, p. arXiv:2110.04270
Vorobyov E. I., Elbakyan V., Hosokawa T., Sakurai Y., Guedel M., Yorke H., 2017, A&A, 605, A77
Watkins E. J., Peretto N., Marsh K., Fuller G. A., 2019, A&A, 628, A21
Wiebe D. S., Molyarova T. S., Akimkin V. V., Vorobyov E. I., Semenov D. A., 2019, MNRAS, 485, 1843
Williams G. M., Peretto N., Avison A., Duarte-Cabral A., Fuller G. A., 2018, A&A, 613, A11
Yang A. Y., Thompson M. A., Tian W. W., Bihr S., Beuther H., Hindson L., 2019, MNRAS, 482, 2681
Zapata L. A., Palau A., Galván-Madrid R., Rodríguez L. F., Garay G., Moran J. M., Franco-Hernández R., 2015, MNRAS, 447, 1826
Zapata L. A., Garay G., Palau A., Rodríguez L. F., Fernández-López M., Estalella R., Guzmán A., 2019, ApJ, 872, 176
Zhang Y., et al., 2019, Nature Astronomy, 3, 517
Zinnecker H., Yorke H. W., 2007, ARAA, 45, 481
van der Walt S., et al., 2014, arXiv e-prints, p. arXiv:1407.6245

This paper has been typeset from a TEX/LATEX file prepared by the author.